Studies in Pure and Transition Metal Doped Indium Oxide Nanocrystals

by

Lisa Nicole Hutfluss

A thesis

presented to the University of Waterloo

in fulfillment of the

thesis requirement for the degree of

Master of Science

in

Chemistry

Waterloo, Ontario, Canada, 2015

AUTHOR'S DECLARATION

I hereby declare that I am the sole author of this thesis. This is a true copy of the thesis, including any required final revisions, as accepted by my examiners.

I understand that my thesis may be made electronically available to the public.

ABSTRACT

Controlling the crystal structure of transparent metal oxides is essential for tailoring the properties of these polymorphic materials to specific applications. Structural control is usually achieved via solid state phase transformation at high temperature or pressure. The first half of this work is a kinetic study of *in situ* phase transformation of In_2O_3 nanocrystals from metastable rhombohedral phase to stable cubic phase during their colloidal synthesis. By examining the phase content as a function of time using the model fitting approach, two distinct coexisting mechanisms are identified — surface and interface nucleation. It is shown that the mechanism of phase transformation can be controlled systematically through modulation of temperature and precursor to solvent ratio. The increase in both of these parameters leads to gradual change from surface to interface nucleation, which is associated with the increased probability of nanocrystal contact formation in the solution phase. The activation energy for surface nucleation is found to be 144±30 kJ/mol, very similar to that for interface nucleation. In spite of the comparable activation energy, interface nucleation dominates at higher temperatures due to increased nanocrystal interactions. The results of this work demonstrate enhanced control over polymorphic nanocrystal systems, and contribute to further understanding of the kinetic processes at the nanoscale, including nucleation, crystallization, and biomineralization.

The ability to further modify the properties of transparent metal oxides through doping of transition metal ions into the host lattice offers a world of possibilities in terms of viable systems and applications. In particular, the use of transition metal dopants to induce room temperature ferromagnetic behaviour in non-magnetic transparent metal oxides is highly desirable for applications such as spintronics. Thus, the second half of this study is concerned with the doping of Fe into nanocrystalline In_2O_3 via colloidal synthesis and the fundamental characterization of the nanocrystals in anticipation of further development of these materials for potential spintronics applications. Focus is placed on the relationship between the doping concentration, observed phase of the host lattice, and nanocrystal growth and properties. Structural characterizations determine that Fe as a dopant behaves quite unlike previously studied dopants, Cr and Mn, establishing a positive correlation between increasing nanocrystal size and increasing doping concentration; the opposite was observed in the aforementioned previous systems.

Through analysis of X-ray absorption near edge structure spectra and the pre-edge feature, it is found that ca. 10% of the assimilated Fe is reduced to Fe^{2+} during synthesis. Magnetization measurements reveal that these nanocrystals are weakly ferromagnetic at room temperature, suggesting the possibility of an interfacial defect mediated mechanism of magnetic interactions. With increasing doping concentration, the decrease in saturation magnetization suggests a change in the magnetic exchange interaction and a consequential switch from ferromagnetic to antiferromagnetic behaviour. It is clear from this work that colloidal Fe-doped In_2O_3 nanocrystals are a promising species, prompting further investigation using additional spectroscopic and magneto-optical techniques to increase understanding of the origin of the observed properties. A thorough understanding of this system in conjunction with other transition metal doped transparent conducting oxides will enable enhanced control in the materials design process and effectively allow tailoring of these materials for specific applications, such as spintronics.

ACKNOWLEDGEMENTS

First and foremost, I thank my supervisor Dr. Pavle Radovanovic for his constant encouragement and support throughout my time in graduate school. His passion for science enabled me to become a better researcher and pushed me to work to the highest level possible, for which I am extremely appreciative. I also thank my committee members, Dr. Scott Hopkins and Dr. Jonathan Baugh, for their effort and time in assisting me during completion of these studies.

I have been fortunate enough to work in a variety of environments with many patient and very talented people. I would like to acknowledge Dr. Ning Chen and Dr. Weifeng Chen at the Canadian Light Source for their assistance with XAS measurements, and Dr. Carmen Andrei at the Brockhouse Institute for Materials Research for her aid in TEM image collection. I also would like to acknowledge the Kleinke lab, and especially Katja Kleinke, at the University of Waterloo for their help and extra accommodation in XRD pattern collection. During my teaching assistantships, I had the pleasure of working with Howard, Sue, and Carey; I learned a lot about leadership from them and am genuinely appreciative of having had these experiences.

I would also like to thank all of my past and present group members in the Radovanovic lab for their encouragement and assistance. In particular, I am grateful to have worked closely with current members Vahid, Terry, Manu, Natalie, and Vadim on a variety of projects and tasks, including running the PPMS for the first time and travelling to the Canadian Light Source. I give special acknowledgement to Natalie for her strong efforts in teaching me the principles of XAS, as well as her willingness to help me with whatever tasks needed completion. It has been a pleasure working with her in the planning of the future steps for this project. I also acknowledge past group members Shokouh and Ting for helping me to get off to a very good start in the lab, their advice and guidance was extremely useful. I am also grateful to have worked with our previous fourth year student, Nicole, as she was highly instrumental in the advancement of the iron doped indium oxide project during the earliest stages.

Last but certainly not least, I am extremely grateful for having such a strong and loving support network of family and friends. I could not have come this far without the reassurance of

my parents and my sister, Amanda, especially during the more challenging moments. I also would not have had half as much fun if it weren't for my friends and hockey teammates. My cat, Luna, has been my constant companion during graduate school, particularly throughout the writing of this thesis, and I am grateful to have her. Finally, I feel incredibly fortunate to have the love and support of Vadim, who understood better than anyone the challenges faced and was always there for me when I needed him most.

CONTENT

LIST OF FIGURES

LIST OF TABLES

LIST OF ABBREVIATIONS

bcc	Body-centred cubic
CLS	Canadian Light Source
DMS	Dilute magnetic semiconductor
DMO	Dilute magnetic oxide
eq	Equation
EXAFS	Extended X-ray absorption fine structure
FT	Fourier Transform
HR-TEM	High resolution transmission electron microscopy
ICP-AES	Inductively coupled plasma atomic emission spectrometry
IN	Interface nucleation
ITO	Indium tin oxide
JMAEK	Johnson-Mehl-Avrami-Erofeev-Kolmogorov
lcp	Left circularly polarized
LMCT	Ligand to metal charge transfer
MCD	Magnetic circular dichroism
MLCT	Metal to ligand charge transfer
NC	Nanocrystal
PPMS	Physical properties measurement system
rcp	Right circularly polarized
rh	Rhombohedral
SN	Surface nucleation
TCO	Transparent conducting oxide
TEM	Transmission electron microscopy
TM	Transition metal
TOPO	Tri-n-octylphosphine oxide
UV-vis	Ultraviolet-visible
XANES	X-ray absorption near edge structure
XAS	X-ray absorption spectroscopy
XRD	X-ray diffraction

Chapter 1 - Introduction*

1.1 Nanomaterials and Transparent Conducting Oxides

The design and tailoring of nanomaterials for specific applications has become an increasingly hot topic as the need for new functional materials grows. The physical properties of semiconductor nanocrystals (NCs) differ from those of the bulk materials due to the effects of quantum confinement; by restricting the size and shape of the crystals such that they are on the same nanometer length scale as the distance within an excited electron-hole pair (exciton), the region in which these charge carriers can travel is reduced and the energy required to excite an electron from the valence band to the conduction band (band gap) is increased.[1,2] This relationship between the band gap and particle size allows for the tunability of nanoscale materials electronic structure for potential applications. An added benefit to working with nanomaterials is the convenient synthetic methods, such as solution-phase synthesis to obtain a suspension of NCs (colloids)[1] which can be precipitated as a solid or cast as a thin film. Nanomaterials boast a wide range of applications, ranging from electronics to drug delivery, and thus have taken centre stage in materials design research.

Transparent conducting oxides (TCOs) are an interesting class of materials as they are transparent in the visible region, chemically stable, and exhibit relatively high conductivity.[3] Additionally, these materials are often polymorphic and exhibit different physical properties depending on the phase obtained, adding another level of complexity to the materials design process.[4-7] Much research has been conducted on a variety of polymorphic TCO nanocrystalline systems, including In_2O_3[8-12], ZnO[13,14], TiO_2[7,15-17], and V_2O_3[5,18]. These studies are motivated by the prospect of enhancing the NCs physical properties and thereby expanding potential applications, illustrating that properties such as conductivity, absorption, and magnetism can be manipulated through lattice defects, dopant incorporation, and NC size.[8,9,19-21] Industrially important metal oxides, including In_2O_3, ZnO, SnO_2, and indium tin oxide (ITO), are utilized in a variety of applications, including thin film photovoltaics and solar cells, liquid crystal and touch

* This thesis contains work that has been published elsewhere.

screen displays, light emitting diodes in solid state lighting, transparent electrodes and transistors, and sensor devices.[3,4,21,22]

Indium oxide, In_2O_3, is an n-type TCO semiconductor with a relatively wide band gap, ~3.75 eV, it exhibits transparency in the visible region, and is capable of high charge carrier concentration.[8,23] As previously discussed, it is technologically important and In_2O_3 in particular is often found in transparent electrodes, sensors, and displays. In_2O_3 has two distinct phases, the metastable rhombohedral corundum structure (rh-In_2O_3; Fig 1.1a) and the stable cubic bixbyite phase (bcc-In_2O_3; Fig 1.1b).

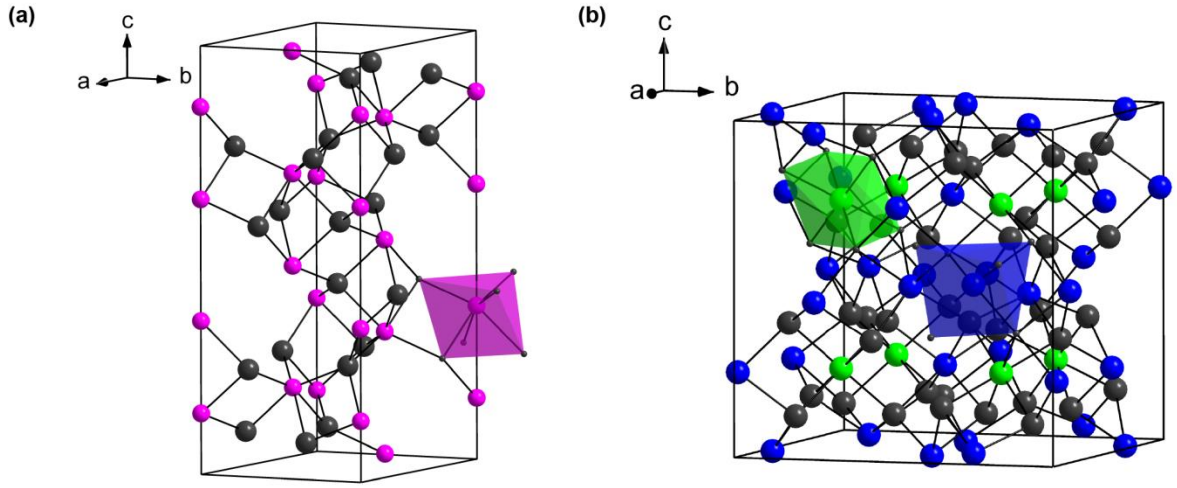

Figure 1.1: Crystal structures of (a) metastable rhombohedral and (b) stable cubic bixbyite In_2O_3. For the rh-In_2O_3 structure, purple and dark grey spheres indicate indium and oxygen atoms, respectively. The b and d sites of bcc-In_2O_3 are indicated by green and blue spheres, respectively, oxygen is again dark grey.

The corundum phase is of space group $R\bar{3}c$, indium occupying two-thirds of the six-coordinate cation sites and oxygen anions forming a hexagonal close-packed lattice.[8,24,25] Given its metastable character, the corundum phase has traditionally only been accessible under high temperature and high pressure conditions in solid state synthesis;[24] as a specific example, it has been shown that bulk rh-In_2O_3 can be obtained at 1250 ^oC and 6.5 GPa.[26] More recently, rh-In_2O_3, as well as rh-ITO, has been achieved under ambient pressure and relatively lower

temperatures using various synthetic techniques.[10,11,23,27,28] The stable cubic phase, space group $Ia\bar{3}$, is similar to the fluorite crystal structure, having one quarter of the anions removed and those remaining are shifted.[9] bcc-In_2O_3 has two six-coordinate sites, designated by Wyckoff notation, in which the indium cations reside; the b-sites, where In^{3+} is somewhat trigonally compressed and of D_{4h} symmetry, and the d-sites, where the octahedral coordination is highly distorted.[9,25] One-quarter of the indium cations occupy the b-sites, while three-quarters occupy the d-sites.[9] As it is the stable phase under ambient conditions and is thus easily isolated, many studies and applications are based on bcc-In_2O_3. However, more convenient routes to obtain rh-In_2O_3 provide more opportunity for application of this material as well as making In_2O_3 an excellent model system for phase transformation studies.

1.2 Phase Transformation and Kinetics

An inherent advantage of working with nanoscale materials is the ability to capitalize on the inverse relationship between NC size and intrinsic surface stress in order to control the crystal structure. It is possible to stabilize high energy crystal structures via sufficient surface stress, and in the case of strongly reduced NC sizes, the resulting high surface area to volume ratio can produce sufficient surface stress to secure such a phase.[8,9,29-31] Consequently, metastable phases can be realized below a specific NC size.[7-9] Previous studies have clearly demonstrated that the observed phase of In_2O_3 NCs is strongly correlated with particle size; the critical size for phase transformation of In_2O_3 NCs has been identified as 5 nm, rh-In_2O_3 being observed in NCs 5 nm or smaller in size.[8,9,32] Thus, nanomaterials with a well-defined phase can be prepared via size control, provided the critical NC size for phase transformation is known. A more traditional route to phase control in bulk materials is through application of pressure,[26,33] and more recently this method been applied to nanoscale systems as well.[34,35] Temperature is yet another critical parameter in overcoming energy barriers to phase transformation in both bulk and nanoscale systems,[26,36,37] and interestingly can be used to manipulate the mechanism of phase transformation.

Modelling of nucleation and growth processes in solid state systems has been extensively studied, leading to the development of numerous models that take into account influential factors

such as conversion fraction, temperature, and number of nucleation sites.[38-43] These models quantitatively and qualitatively describe reaction kinetics in solid state materials. Models based on the theoretical concepts developed by Avrami in the early 1940s are most common and generally applicable to phase transformation processes.[43-45] The Johnson-Mehl-Avrami-Erofeev-Kolmogorov (JMAEK) model is distinguished by its consideration of nuclei ingestion and coalescence, as well as its ability to accurately determine the activation energy for a variety of systems in spite of seemingly limiting assumptions made during derivation.[32,43,45] For instance, the JMAEK model assumes that the system is infinite in size, which is clearly not the case for nanoscale materials, and yet this model has been successfully applied to NC phase transformation nonetheless.[32] In the late 1990s and early 2000s, the surface and interface nucleation models were developed by Zhang and Banfield in order to describe the solid state phase transformation of anatase to rutile nanoparticles in the powder form.[7,37,46] While there have been many reports on phase transformation in powder systems and TiO_2 in particular, there remains much work in furthering the understanding of phase transformation in colloidal nanoparticles. The interface nucleation model has since been applied to colloidal In_2O_3 NCs and was found to accurately detail the transformation from rhombohedral to cubic phase under the given temperature and precursor conditions.[32] Given the applicability of that particular Zhang and Banfield model in this system, further investigation into other mechanisms of phase transformation in colloidal solution is warranted.

Interface nucleation (IN) involves the formation of a nucleation site at a particle-particle contact point, after which the new phase rapidly consumes the two particles (Fig. 1.2a). By contrast, surface nucleation (SN) relies on the formation of nucleation sites on individual particle surfaces via random thermal fluctuations in order to initiate phase transformation (Fig. 1.2b). Additionally, these two mechanisms can simultaneously be at work, giving rise to a combined mechanism (IN+SN). The activation energies for IN and SN differ; in IN, interfacial defects such as lattice vacancies or dislocations generally result in lower energy barriers to the transformation to a more stable state. Temperature, particle size, and packing density of particles have been found to have a strong influence on the mechanism by which the transformation occurs and thus the activation energy required to complete the transformation.[7,37,46]

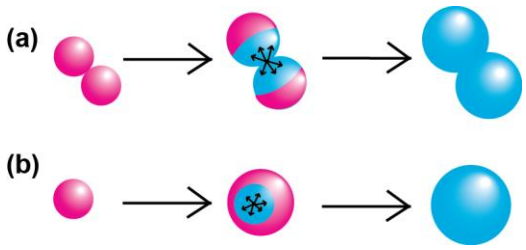

Figure 1.2: Schematic representation of (a) interface and (b) surface nucleation mechanisms of phase transformation. Pink spheres represent the initial phase, while blue spheres represent the final phase. Nucleation sites are indicated by black arrows. Change in size of the spheres indicates particle growth accompanying the phase transformation.

In the derivation of the kinetic models of phase transformation, it has been shown that the equations for different models could be rearranged such that the left hand side is common to all expressions, and this portion was subsequently denoted as y (eq 1.1).

$$y = \frac{(D_{rh} / D_o)^3}{(1-\alpha)} - 1 \qquad (1.1)$$

Here, α is the fractional cubic phase content, D_{rh} represents the average rhombohedral NC size in terms of the diameter at a given time, and D_o the initial average rhombohedral NC diameter, which is taken to be the rh-In_2O_3 NC size at the earliest time point in the reaction. The IN and SN models are given by eqs 1.2 and 1.3, respectively,

$$y(\mathrm{IN}) = k_{\mathrm{IN}} N_o t_x (1 - e^{-t/t_x}) \qquad (1.2)$$

$$y(\mathrm{SN}) = e^{k_{\mathrm{SN}} t} - 1 \qquad (1.3)$$

where t is time in both cases, k_{IN} and k_{SN} are the interface and surface nucleation rate constants, respectively. In eq 1.2, N_o is the initial number of rhombohedral particles (often shown combined with k_{IN}), and t_x is the time at which the IN mechanism no longer contributes to phase transformation and the function levels off. The coexistence of IN and SN mechanisms can be represented simply by the sum of eqs 1.2 and 1.3, which is an approximation for the combined

mechanism.[37] In particular, the sum of eqs 1.2 and 1.3 was utilized in the TiO_2 phase transformation study, in which Al_2O_3 particles served as a spacer between TiO_2 particles, mimicking dilute conditions in the nanopowder form.[37] The short-time linear behavior and long-time exponential behavior of experimental data is indicative of IN dominance at short times and SN dominance at long times in the combined model. In addition to taking the sum of eqs 1.2 and 1.3, a combined model was also derived to describe phase transformation by mixed mechanisms (eq 1.4).[37] This expression is shown to accurately fit the experimental data involving both mechanisms under ideal conditions. It can be seen that as the IN contribution diminishes, $k_{IN}N_o$ approaches zero and the remaining portion of the equation is that of SN alone (eq 1.3 above). Furthermore, for either very long or very short times, eq 1.2 can be reduced to $y(\mathrm{IN}) = k_{IN}N_o t$, which is the ideal form of the IN mechanism.[32,37]

$$y(\mathrm{IN}+\mathrm{SN}) = (1+\frac{k_{IN}N_o}{k_{SN}})(e^{k_{SN}t}-1) \qquad (1.4)$$

Using experimentally determined α, D_{rh}, and D_o values, eq 1.1 can be employed to obtain the experimental y values as a function of time for a given set of samples. By then fitting these data with the kinetic model equations, the mechanism responsible for phase transformation can be identified based on which model best fits the experimental data. Given the different functional forms of the models, the IN and SN mechanisms appear quite distinct when plotted. Figure 1.3 demonstrates calculated curves for IN, SN, and the literal sum of the two mechanisms as a function of time.

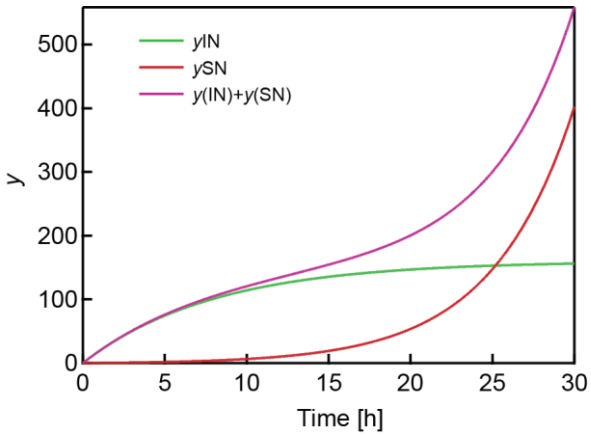

Figure 1.3: Sample calculation curves illustrating the distinctive appearances of y(IN), y(SN), and the sum of the two mechanisms over the course of 30 h. In this example, k_{SN} is 0.2 h^{-1}, $k_{IN}N_o$ is 20 h^{-1}, and t_x is 8 h. y is defined by eq 1.1.

The activation energy of the phase transformation process can be obtained through application of the Arrhenius equation (eq 1.5), which describes an empirical relationship between the temperature of the reaction and the rate constant.[47] Here, k is the rate constant of the reaction, A_o is the pre-exponential factor, E_a is the activation energy, R is the ideal gas constant, and T is the temperature.

$$k = A_o e^{-E_a / RT} \tag{1.5}$$

Quite often, the natural logarithm of the Arrhenius expression is taken and used to plot ln(k) as a function of T^{-1}, thus making this a linear relationship and enabling extraction of the activation energy (eq 1.6).

$$\ln(k) = \ln(A_o) - \frac{E_a}{RT} \tag{1.6}$$

It has also been shown that eq 1.6 can be rearranged in order to provide an estimate for the activation energy when only two sets of k, T data are available (eq 1.7).[37]

$$E_a = \frac{T_2 T_1}{T_2 - T_1} R \ln\left(\frac{k(T_2)}{k(T_1)}\right) \tag{1.7}$$

It is known that interface and surface nucleation have different activation energies, SN being a much higher energy process. In the original study, it was found that the anatase-to-rutile phase transformation in nanocrystalline TiO_2 had an average activation energy of 170 kJ/mol by IN, while that for SN was 466 kJ/mol.[37] Previous work with colloidal In_2O_3 has shown that the average activation energy for IN phase transformation in this system is 152 kJ/mol.[32] Thus it is anticipated that SN in colloidal In_2O_3 would be of higher activation energy than that of IN, and identification of the conditions leading to either mechanism would allow for enhanced control over the phase transformation process.

1.3 Dilute Magnetic Semiconductors, Oxides, and Magnetic Behaviour

The previous discussion regarding phase transformation can be extended to doped systems, materials in which a dopant impurity has been intentionally incorporated into the host lattice, resulting in modification of the physical properties. The presence of a dopant can influence the structure of the host lattice, providing the potential to favour a phase that otherwise would not be readily accessible in the pure material. Isolation of a new phase with distinctive properties can lead to new applications of these materials, which in itself is a motivation for study. The impact of the dopant on lattice structure in addition to its influence on the optical, electronic, and magnetic properties of the system makes doping an attractive method by which a material can be tuned for a specific application. ITO is a classic example of utilizing dopants to enhance optical and electronic behaviour of NCs; the incorporation of tin into the indium oxide host results in a metallic character, achieving high conductivity and low resistivity while maintaining chemical stability and high transmission in the visible region.[21,48,49] Polymorphism in indium oxide has also been exploited in ITO studies, both the cubic bixbyite and rhombohedral phases being achieved under relatively mild synthetic conditions.[28,50] Given these properties, ITO is an industrially important material as it can be used in a variety of applications including, but not limited to, flat panel displays, light emitting diodes, gas sensors, and window coatings.[21,28,48-50]

Just as the incorporation of dopants to enhance optical and electronic properties is a major area of study, imparting magnetic behaviour to a host material through doping is another highly relevant research field. Dilute magnetic semiconductors (DMSs) are an important class of

materials in which magnetic elements have been doped into non-magnetic semiconductors.[51-53] Ideal synthesis and tuning of DMSs results in materials that have the best of both worlds; they retain characteristic semiconductor properties while also exhibiting room temperature ferromagnetism. Applications such as spintronics, which will be discussed in greater detail, rely on utilization of both the electron charge and spin degrees of freedom, thus providing a prime motivation for the development of DMSs.[54] Specifically, a material that is suitable for spintronics should only undergo the change from ferromagnetic to paramagnetic at a temperature (Curie temperature, T_C) which is well above room temperature[55,56]; this change is induced by the thermal disruption of the spontaneous spin alignment. Additionally, the exhibited ferromagnetism should be intrinsic, as opposed to being the result of an extrinsic source, such as isolated clusters of magnetic material.[55,56] Pure metals that exhibit magnetic behaviour, for example iron, are not suitable for such applications for many reasons, most notably because the conductivity cannot be tuned through doping, in addition to increasing resistivity with increasing temperature.[55] On the other hand, materials such as pure TCOs are not utilized in spintronics as they lack ferromagnetic behaviour. Magnetic materials including species of transition metal oxides and spinels offer a very broad avenue to possible spintronics devices, some examples being chromium-based chalcogenides and ilmenite-hematite thin films.[57,58] This category of materials is quite vast and offers a wide range of properties which can be tuned through composition or techniques, such as the layering of different materials, to modify the electronic structure at the interfaces and thereby enable achievement of the desired properties.[59-62] With all of these considerations, DMSs and dilute magnetic oxides (DMOs) in particular remain an attractive option for spintronics applications because they combine traditional semiconductor properties and magnetism within a single homogeneous material. Much work has been invested into their development over the past several decades and it has become an increasingly popular research area as successes in synthesis and tunability of these materials are observed.

There is still much debate regarding the mechanisms which lead to magnetic interactions within DMO materials, particularly in observed room temperature ferromagnetism. The typical mechanisms of magnetic exchange interactions, such as double exchange and superexchange, are short-ranged and thus make it difficult to understand how DMOs are capable of magnetic ordering other than paramagnetism.[63] In some cases, the observed magnetic behaviour can be attributed to extrinsic sources, such as secondary phases or other contaminants; however,

external materials are not always the cause, and further explanations have been developed. Magnetic behaviour in DMOs has often been attributed to the presence of defects within the lattice, in particular oxygen vacancies[64,65], and as a consequence many of these mechanisms heavily involve defects. In the bound magnetic polaron model, exchange interactions between TM dopant electrons are mediated by spin polarized carrier electrons, which are trapped in narrow defect bands.[66,67] Alternatively, mobile charge carriers, as opposed to trapped carriers, can also mediate interactions between localized TM electrons in a carrier-mediated model.[67] Relatively recently, a charge transfer mechanism of magnetic interaction was developed in which a spin-split defect band can give rise to ferromagnetic coupling when dopant TMs of differing oxidation states undergo charge transfer, thereby contributing electrons to the defect density of states and spin-splitting.[67-70] Given the correlation between observed magnetic behaviour and defects, the method of sample preparation is often linked to the observed magnetic properties as it can strongly influence the amount of oxygen vacancies.[20,71] Obtaining experimental evidence as to which mechanism is most likely at work poses an additional challenge in analysis and development of DMOs.

As mentioned, thorough investigation of DMS and DMO materials is strongly motivated by their potential application in spintronics. This field of research is concerned with elucidating the interaction between the electron spin and its environment, ultimately leading to the development of devices which make use of this relationship.[54] Key challenges faced include methods of introducing spin polarized electrons to the system, determination of how long the spin orientation can be maintained, and lastly, detection of the spin polarization.[54] Considering a conceptual spin field-effect transistor as an example and taking a simplistic viewpoint, a ferromagnetic source injects spin polarized electrons through a narrow channel, which travel ballistically towards a ferromagnetic drain.[54,72] Electrons may pass into the drain provided the spin direction is the same as that of the drain, and in which case the current can flow and the gate is open; otherwise, current cannot flow and the gate is closed.[54] Manipulation of the applied voltage influences the effective magnetic field experienced by the electrons, in turn affecting spin precession and thus allowing for gate control.[54] From the materials chemistry perspective, nanoscale uniform DMS and DMO systems as well as heterogeneous DMSs provide a platform through which spontaneous spin polarization and electron conduction can be manipulated, and thus thorough examination of such materials is required.[73]

1.4 Iron-Doped Indium Oxide

First row transition metals (TMs) are often used as dopants in non-magnetic metal oxide semiconductors and insulators in order to impart ferromagnetic behaviour.[51,53] The physical properties of indium oxide which make it a scientifically interesting and technologically important material have already been discussed in section 1.1, and many studies have been completed using indium oxide as a host lattice for various dopants.[6,9,74-76] Given that iron is magnetic and highly soluble in the indium oxide lattice, Fe-doped indium oxide in particular is a promising material for future spintronics devices and thus the development of this material is of great interest.[20,77-80]

The two phases of indium oxide offer multiple sites in which a dopant can be substitutionally incorporated. In bcc-In_2O_3, Fe can be substituted for In in either the b- or d-sites, and in rh-In_2O_3 a dopant can reside in the In c-site. In a 6-coordinate environment, the ionic radius of In^{3+} is 0.80 Å, while Fe^{2+} and Fe^{3+} have ionic radii 0.61 and 0.55 Å, respectively,[81] thus indicating that either oxidation state of Fe could easily substitute for In. It follows that the lattice shrinks accordingly with the incorporation of Fe, which has been confirmed in previous works.[20,79]

Iron(III) oxide is a polymorphic material with four phases, namely the most common forms hematite (α-Fe_2O_3) and maghemite (γ-Fe_2O_3), as well as the far less abundant β-Fe_2O_3 and ε-Fe_2O_3 phases.[82] The favoured α-Fe_2O_3 has a rhombohedral structure and the relatively unstable β-Fe_2O_3 has a cubic bixbyite type lattice, β-Fe_2O_3 having only been identified in nanocrystalline form[82]; interestingly, these trends in phase stability are opposite that of In_2O_3. Studies in phase transformation and stability of nanocrystalline Fe_2O_3 are of wide interest considering that the different phases have applications in heterogeneous catalysis, biochemistry, and magnetism[82-84], in addition to the appearance of these metal oxides in geological and planetary investigations.[85]

Many experimental and theoretical studies have focused on Fe-doped In_2O_3, whether in the form of NCs or thin films, for the previously discussed motivations.[67,78,86] One challenging aspect of this system is the plethora of conflicting reports regarding the type of magnetism observed; this is not uncommon in DMS and DMO systems in general, and often the synthetic methods and sample treatments play a pivotal role in the observed magnetic behaviour and thus the associated mechanism of interaction. For instance, room temperature ferromagnetic

behaviour has been reported for nanocrystalline Fe-doped In_2O_3[77,78], however paramagnetic behaviour has also been observed in both bulk and nanocrystalline samples[87-89]; synthetic methods vary and include pulsed laser deposition, coprecipitation, and solid state techniques. Given the relationship between defects, oxygen vacancies, and magnetism, many studies have linked high temperature annealing with reduced oxygen vacancies and decreased ferromagnetic signal.[90] It has also been shown that variations in oxygen partial pressure during pulsed laser deposition synthesis can directly manipulate magnetic behaviour through oxygen vacancies.[86] Theoretical studies further solidify these findings, solidifying the link between oxygen vacancies and magnetic behaviour in Fe-doped In_2O_3.[64,67]

1.5 Purpose of Research

In a broader context, this research aims to increase understanding of nanocrystalline colloidal systems in the hopes that these concepts can lead to the development of functional nanomaterials for applications such as spintronics. This is of importance because without a solid understanding of the driving forces behind these systems, they cannot be effectively manipulated in order to achieve a desired result. In the future, this knowledge can be extended not only to other TCO semiconductor systems, but to help increase understanding of processes such as biomineralization.

Specifically, the first half of this work is concerned with elucidating and controlling the mechanisms by which phase transformation occurs in colloidal indium oxide NC solutions. Examining the kinetics of phase transformation paves the way for achieving enhanced control over structure and properties such as NC size, morphology, phase, and optical properties, which is essential for the materials design process. Exploring the *in situ* phase transformation in solution also provides the opportunity to establish the correlation between NC growth and phase transformation, while eliminating the influence of substrate, nanoparticle spacers, aggregation or other effects which are unavoidable in powder phase studies. The impact of factors including synthesis temperature, precursor to solvent ratio, and time are quantified in a manner that enables complete tailoring of the resultant NCs.

The second portion of this research focuses on the doping of colloidal indium oxide NCs with iron. The main goal in this work is to establish successful synthetic routines and conduct the standard characterizations in the context of dopant influence on NC growth, phase, and properties, as well as set the stage for future studies and material development. This will add to the current database of DMS nanomaterials and provide further insight into how different dopants alter the properties of the same host lattice. Once again, the importance of demonstrating tunability of the material properties comes into play as the prospect of potential future application in spintronic devices is a strong motivation. Thus, an understanding of how the preparation methods affect the observed properties is also of great interest in this project, particularly since DMOs are notorious for exhibiting different properties depending on the preparation method.

In the case of both projects, nanocrystalline indium oxide is the semiconductor of choice based on its technological relevance in addition to its chemical stability. The presence of two phases allows for examination of phase transformation without invoking too many variables, as would be the case for substances which exhibit more than two phases. It also enables examination of the dopant-host relationship in the context of phase transformation. Finally, indium oxide is a well characterized material, and thus many comparisons with literature involving different synthetic methods and dopants are possible. Iron is employed as the doping agent since it is known to be a strongly magnetic TM and so the likelihood of observing ferromagnetic behaviour is greater. Similarly to indium oxide as a host, iron is a commonly employed TM dopant and its application here provides opportunity for comparison and increased understanding of the role iron plays as a dopant.

Chapter 2 – Experimental Methods

2.1 Materials

All solvents and reagents were used as provided by the manufacturer. No further purification was performed. Indium acetylacetonate ($In(acac)_3$; 98%) was purchased from STREM Chemicals. Iron(III) chloride ($FeCl_3$; 97%), oleylamine (70%), and tri-n-octylphosphine oxide (TOPO; 90%) were purchased from Sigma Aldrich. Solvents utilized include toluene (EMD Chemicals; 99.98%) and absolute ethanol.

2.2 Synthetic Methods

2.2.1 Synthesis of Pure Indium Oxide Nanocrystals

The In_2O_3 NC synthesis has been previously reported and was further modified for this study.[8,32] 6.11 mmol of $In(acac)_3$ and 122 mmol of oleylamine were combined in a 100 mL round-bottom flask to give a 1:20 molar ratio of precursor to solvent. In subsequent reaction sets, the amount of oleylamine was reduced to obtain 1:16 and 1:12 precursor to solvent molar ratios. The reflux system was assembled and the mixture was degassed with stirring for 15 min. The mixture was then heated to the desired reaction temperature over the course of 1 h. Both the external and internal flask temperatures were recorded regularly throughout pre-heating and reaction time periods. The average internal flask temperature from the reaction start to finish was taken as the true temperature in further analysis.[91] For all reactions, an identical setup and the same equipment (flask, thermometer, and stirring bar) were utilized. By sensitive adjustment of the heat settings and continuous temperature recording throughout the duration of the reaction, the temperature fluctuations were limited to ca. ±2.5 °C. Samples were extracted at designated times using a glass syringe, placed in a test tube and promptly sealed with parafilm. Once the final reaction time was reached, the sample was removed from heat and cooled naturally to room temperature while continuing stirring under argon. The colloidal samples were precipitated with ethanol and isolated through centrifugation at 3000 rpm for 5 min. The supernatant liquid was discarded, and the washing process with ethanol was repeated two more times. A portion of the final samples were preserved in ethanol, while the majority of the material was dried and crushed

into a fine powder. The precipitated samples held in ethanol were centrifuged, combined with an approximately equivalent volume of TOPO, and stirred in a 90 ^{o}C oil bath for 1 h. After the treatment was complete, the samples were precipitated and washed with ethanol. The TOPO treatment was repeated, if necessary, and the NC product was finally suspended in hexane to form clear colloidal suspensions.

2.2.2 Synthesis of Iron-Doped Indium Oxide Nanocrystals

The preparation of doped colloidal In_2O_3 NCs has been reported for Cr and Mn dopants[9,92]; these techniques were modified for synthesis with Fe as the dopant. In a 100 mL round bottom flask, 1.94 mmol of $In(acac)_3$ was combined with 23.3 mmol of oleylamine and 0.0971 mmol of $FeCl_3$ for synthesis of a 5 mol% Fe sample. The In precursor to oleylamine solvent molar ratio in all cases was 1:12. For higher doping concentrations, the amount of $FeCl_3$ was increased relative to the molar amount of In. The orange-yellow coloured mixture was degassed with stirring under argon and reflux for 10 min, after which it was heated to the desired temperature over the course of 1 h. The reaction was then held at constant temperature for 1 h. Both external and internal flask temperatures were recorded every 5 min during the pre-heating and reaction time periods, the average of each temperature data set being taken as the true external and internal reaction temperatures. Once the reaction time was complete, the transparent yellow solution was removed from heat and allowed to cool to room temperature naturally with continued stirring under argon flow and reflux, becoming increasingly opaque. The solution was then divided equally between two test tubes. Equivalent amounts of ethanol were added to each solution to precipitate the doped NCs, which were then isolated through 5 min of centrifugation at 3000 rpm. The supernatant liquid was discarded and the washing process repeated two more times. After the final washing, TOPO was added to each sample in an approximately volume equivalent amount. The samples were then placed in a 90 ^{o}C oil bath and stirred for 1 h, after which they were allowed to cool and subsequently washed with ethanol. The TOPO treatment was repeated two more times, after which one of the samples was dried and crushed to a fine, yellow powder. Most of the sample in the second test tube was dispersed in toluene to produce a transparent, yellow solution, and a very small portion was dispersed in hexane to give a transparent, faint-yellow to colourless solution.

2.3 Characterization Techniques

2.3.1 X-ray Diffraction

X-ray diffraction (XRD) patterns were collected with an INEL XRG 3000 powder X-ray diffractometer using Cu Kα radiation source (λ = 1.540598 Å), germanium crystal monochromator, and an INEL CPS 120 curved position sensitive detector operating at 30 kV and 30 mA. Powder samples were loaded into an aluminum sample holder, and each pattern was collected for up to 2 h to obtain sufficiently high signal-to-noise ratio.

2.3.2 Transmission Electron Microscopy

The samples were prepared for transmission electron microscopy (TEM) imaging by diluting a small portion of the toluene-dispersed samples, followed by extensive sonication and further dilution if necessary. Samples were then deposited on copper grids with lacey Formvar/carbon support films purchased from Ted Pella, Inc. TEM images were collected using a JEOL-2010F microscope operating at 200 kV at McMaster University.

2.3.3 Inductively Coupled Plasma Atomic Emission Spectrometry

Samples were prepared for inductively coupled plasma atomic emission spectrometry (ICP-AES) analysis by digesting a known sample mass in a small quantity of aqua regia, followed by sonication. The aqua regia solution was prepared immediately prior to use by combining small volumes of nitric and hydrochloride acids in a 1-to-3 parts ratio. All steps involving aqua regia were completed solely in the fume hood. Once digested, samples were diluted with deionized water in volumetric flasks. An indium standard was prepared by dissolving $InCl_3$ in deionized water. ICP-AES analysis was completed at the University of Guelph.

2.3.4 UV-vis Absorption Spectroscopy

UV-vis electronic absorption spectra were collected using a Varian Carey 5000 UV-vis-NIR spectrophotometer and quartz cuvettes (Spectrosil, Starna Cells, Inc.) with transparency range 170 – 2700 nm and 1 cm optical path length. Samples dispersed in hexane were employed for these measurements.

2.3.5 X-ray Absorption Spectroscopy

X-ray absorption spectroscopy (XAS) measurements were completed at the 06ID-1 beamline at the Canadian Light Source (CLS) using liquid nitrogen-cooled double crystal monochromator, consisting of two crystal pairs (Si (111) and Si (220)). A Sn foil standard (K-edge at 29200 eV) was used for indium K-edge energy calibration for measurements with pure In_2O_3 samples. An Fe foil standard (K-edge at 7112 eV) was used for iron K-edge energy calibration when measuring Fe:In_2O_3 samples. In the case of pure In_2O_3 samples, spectra were recorded in transmission mode with three ionization chambers, the first two of which monitored the incident and transmitted X-ray intensities, respectively, while the third was used as additional internal calibration for the In K-edge position. When measuring Fe:In_2O_3 samples, fluorescence mode and a 32 channel germanium detector were used to collect spectra.

2.3.6 Magnetization Measurements

Magnetization of the materials was measured for nanocrystalline films rather than for free-standing NCs. Quartz substrates were cut to approximately 5 mm in length and width, followed by sonication in aqua regia for 2 h. After this point, substrates were considered to be part of the sample and thus only handled with non-magnetic, Teflon-coated tweezers. The mass of each substrate was recorded in triplicate prior to sample deposition. Double sided tape was used to secure a substrate to the spin coater, the rough side of the quartz facing up, and a drop of colloidal NCs in toluene was deposited. The sample was then spun at ca. 200 – 300 rpm for a total of 2 min, followed by annealing in an oven at 300 ^{o}C for 1 min. The sample was allowed to cool for 3 min, and was again secured to the spin coater. This process was repeated a total of 10 times, after which the mass of the substrate with sample was taken in triplicate. Once the sample

had reached a minimum mass of 1 mg, the process was either continued or considered complete; ideal sample masses ranged from 2 – 5 mg. For each sample type, three substrates of different masses were prepared. The sample coated substrate was wedged inside a plastic capsule such that it did not move when shaken. The two halves of the capsule were secured with two layers of Kapton tape and inserted into a plastic straw up to a pre-determined depth. For added security, a small amount of Kapton tape was placed over the end of the straw to prevent the capsule from being lost in the instrument in the rather unlikely event that it was shaken loose during measurements.

A physical properties measurement system (PPMS, Quantum Design) in ACMS mode with a helium cooling system was employed for magnetization measurements of the samples. The magnetometer is capable of collecting data at temperatures ranging from 2 – 400 K and fields ranging from ± 9 T. In this particular series of experiments, sample magnetization was measured as a function of the applied field at 300 K and fields ranging from ± 5000 Oe. As a brief overview of instrument schematics, a superconducting drive coil surrounds the detection coils in a longitudinal set up, and the sample is inserted into the space within the coils via a long, thin rod. A series of compensation and calibration coils are incorporated into the ACMS coil set in order to reduce background noise and ensure accurate measurements, and a non-magnetic thermometer is present for temperature measurement. The detection coils work by measuring changes in the applied magnetic field due to the presence of the sample. This set up is collectively referred to as the probe, and it allows for both magnetic field and temperature control. Electronic control of the components and thus execution of measurement sequences are carried out by the Model 6000, which is directly connected to the probe. A personal computer is utilized as an interface between the user and the Model 6000, additionally allowing for data storage upon completion of a measurement.

2.4 Data Treatment

2.4.1 Phase Transformation Studies

All XRD patterns were collected using the same instrument parameters and calibration, and analyzed by linear combination and peak deconvolution upon the background subtraction.

For both analyses, all patterns were baseline-corrected in the 2θ range 25-40° by spline interpolation. Linear combination of XRD patterns has been proven an effective method for the determination of phase content.[32] XRD patterns of pure rh-In_2O_3, bcc-In_2O_3, and InOOH samples synthesized through the same methods as described in section 2.2.1 and having different NC sizes were used as reference materials in the linear combination analysis, where they were added in varied proportions to reproduce the experimental data. Considering that InOOH is a precursor to rh-In_2O_3, calculations involving the rh-In_2O_3 fraction included the InOOH content as well,[8] when this species was present. To account for an error introduced by linear combination analysis, the bcc-In_2O_3 fractional content (bcc content) was considered in terms of the maximum and minimum fraction of bcc-In_2O_3 that would reasonably fit the experimental patterns based on the overall difference between the experimental pattern and linear combination. The average composition was then taken as the true bcc content. For the deconvolution analysis, the same 2θ range was used as for linear combination. The phase contents of In_2O_3 NCs were calculated by fitting the overlapped bcc-In_2O_3 (222) and (400), and rh-In_2O_3 (104) and (110) peaks, allowing for variable broadening of the XRD peaks based on the average NC size.[32] The intensities of the peaks were set proportionally to their standard referenced intensities. The phase content was reported as an average value of the linear combination and peak deconvolution analysis, and the error bars are associated deviations from the average value. Fitting of models to experimental data was performed using the Trust Region algorithm. Extended X-ray absorption fine structure (EXAFS) data analysis was completed as described previously,[32] and the phase content at different times in the reaction was determined by a linear combination of pure phases as references.

2.4.2 Analysis of Doped Materials

The Scherrer equation, eq 2.1, was employed to obtain an estimate of bcc-In_2O_3 particle size. D_{hkl} is the diameter of the particle, in nm, in the direction perpendicular to the hkl lattice plane, B_{hkl} is the full width at half maximum (FWHM) of the XRD peaks in rad, and θ is the Bragg angle.[93] K is the crystallite-shape factor, taken to be 0.9, and λ is the wavelength of the X-rays utilized.[93]

$$D_{hkl} = \frac{K\lambda}{B_{hkl}\cos(\theta)} \tag{2.1}$$

Peaks were fit with a Gaussian function to obtain the FWHM and peak centre using the Origin program. The highest intensity reflection, (222), was used in all calculations.

Gatan DigitalMicrograph software was utilized to measure lattice d-spacings of the high resolution transmission electron microscopy (HR-TEM) images. Particle size distributions were determined via measurement of at least 120 NCs, measured along the largest diameter of each particle.

XAS spectra were prepared for analysis using the Athena software package. Detector channels that did not provide a clean spectrum were identified and excluded, the useful channels being merged; multiple scans of each sample were then also merged to produce one spectrum. The background prior to the edge was subtracted using a first degree polynomial; normalization of the post-edge region was completed using a second degree polynomial. The spectra were then deglitched as necessary and the edge, E_o, identified using a first derivative plot. For X-ray absorption near edge structure (XANES) spectroscopy analysis, baseline corrections of the pre-edge feature were completed in Origin using a spline interpolation function. Fitting of pre-edge features was performed using the PeakFit program. Fitting methods were selected based on literature pertaining to pre-edge fitting of Fe XANES spectra; a Gaussian-Lorentzian area summation function was utilized as a pseudo-Voigt fitting approach, and the contribution of Gaussian and Lorentzian functions to the sum was held at ca. 50% each, while the peak widths were held at ca. 1.4 eV.[94,95] Please refer to Appendix B for a sample calculation of the pre-edge centroid.

Magnetization data were corrected for diamagnetic contributions and centred, enabling extraction of the saturation magnetization.

Chapter 3 – Controlling the Mechanisms of Phase Transformation in Colloidal Indium Oxide Nanocrystals

3.1 Determination of Phase Content

The kinetic investigations of phase transformation were performed by analyzing the change in the phase content during the synthesis of NCs using different precursor to solvent ratios. Unlike nanocrystalline powder, in colloidal suspensions the size and concentration of NCs can be accurately and reproducibly controlled, which is essential for examination of the influence of these parameters on the phase transformation mechanism. Figure 3.1 shows the XRD patterns of the samples synthesized using 1:20 precursor to solvent ratio at 200 and 224 ^{o}C. For the 200 °C reaction temperature (Figure 3.1a), at short times the sample consists of a mixture of rh-In_2O_3 and InOOH with small amounts of bcc-In_2O_3. At longer times, the phase content becomes a mixture of rh-In_2O_3 and bcc-In_2O_3 only, as InOOH undergoes dehydration to form rh-In_2O_3 NCs prior to transformation to the cubic phase. The presence of InOOH and its subsequent disappearance at an early stage of the synthesis is consistent with the cascade dehydration mechanism of In_2O_3 NC formation previously reported (Appendix A, Figure A1).[8,23] The peaks corresponding to rh-In_2O_3 and InOOH are significantly broader than those corresponding to bcc-In_2O_3, suggesting that phase transformation from rh- to bcc-In_2O_3 accompanies NC growth. At higher temperature (Figure 3.1b), the samples display largely bcc-In_2O_3 phase even at short times, with no InOOH present, indicating faster particle formation and phase transformation with increasing temperature.

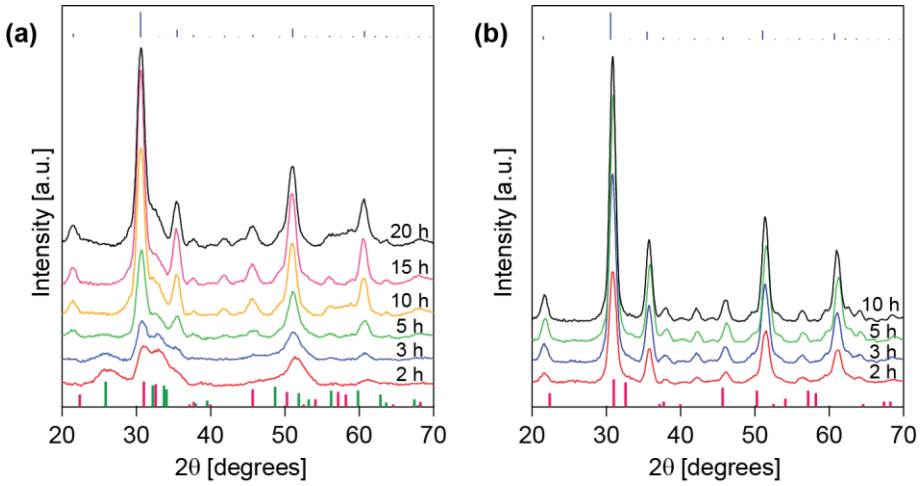

Figure 3.1: X-ray diffraction patterns of samples synthesized at (a) 200 and (b) 224 ^{o}C over the course of 20 h. Precursor to solvent ratio is 1:20. Blue sticks at the tops of the plots indicate the bcc-In_2O_3 reference pattern (JCPDS 06-0416), while pink and green sticks at the bottoms indicate rh-In_2O_3 (JCPDS 21-0406) and InOOH (JCPDS 17-0549) reference patterns, respectively.

Determination of the bcc-In_2O_3 fractional content through linear combination is demonstrated in Figure 3.2a (bottom) for a sample taken at 5 h from the 1:20 precursor to solvent series at 200 ^{o}C. The sharpness of the bcc-In_2O_3 (222) and (400) peaks relative to the broad peaks of rh-In_2O_3 lead to significant changes in the linearly combined pattern with only slight changes in the bcc phase content. The experimental XRD pattern (black line) is in excellent agreement with the pattern corresponding to 42 % bcc phase and 58 % rh phase (green line). These results were confirmed by the peak deconvolution method, as previously described (Figure 3.2a, top).[32] A good agreement is obtained even in cases involving InOOH at the very early stage in the reaction (Appendix A, Figure A2). The average NC sizes necessary for reproducing the peak broadening generally match NC sizes corresponding to the reference patterns for the linear combination. The agreement between the phase content results obtained by deconvolution and linear combination methods is demonstrated in Table A1 (Appendix A). To confirm the results of the XRD analysis, In K-edge EXAFS spectroscopy, which is sensitive to the local

environment of In sites, was employed and can also serve as a quantitative measure of the phase content. Figure 3.2b shows a selected EXAFS spectrum of a sample prepared at 200 °C for somewhat later time into the reaction (green), together with the spectra of pure rh-In_2O_3 (pink) and bcc-In_2O_3 (blue) NCs as references. The linear combination analysis (black line) reveals ca. 20 % bcc phase content which is in good agreement with XRD analysis (15 %). Figure 3.2c plots the bcc-In_2O_3 content of the 1:20 precursor to solvent series over time, illustrating that the conversion from rh-In_2O_3 to bcc-In_2O_3 is accelerated with increasing temperature, as anticipated. Under isothermal conditions, the rate of reaction decelerates with time at any given temperature. This observation applies to other dilution series, although the overall rate of phase transformation is strongly dependent on the solvent to precursor ratio (Appendix A, A3). The bcc-In_2O_3 content, α, can then be utilized in kinetic modelling of the phase transformation process according to previously developed models.[32,37]

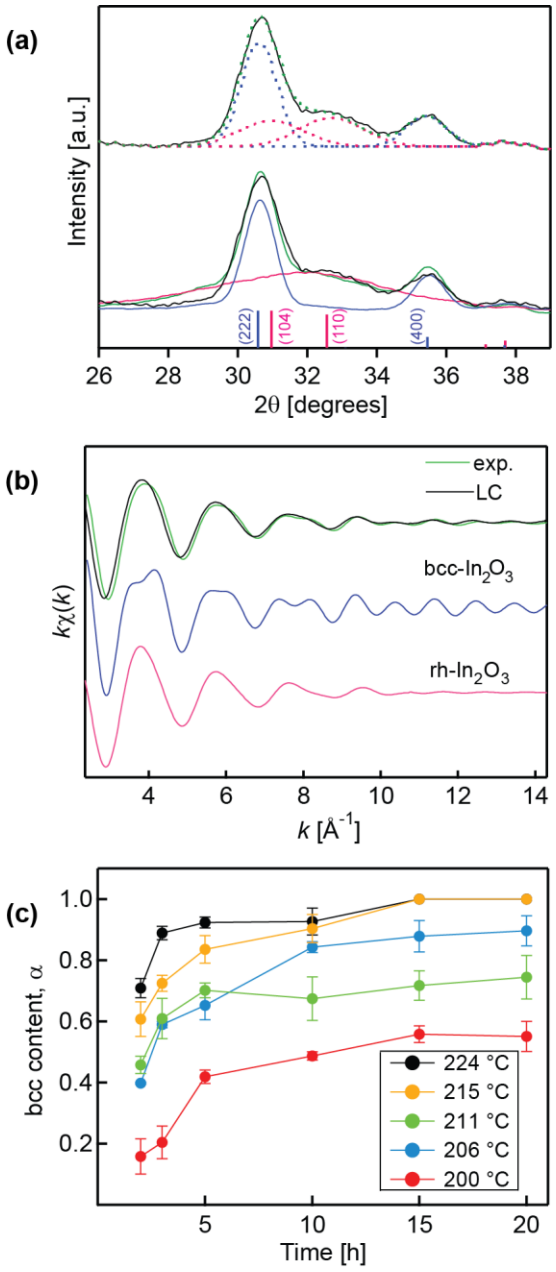

Figure 3.2: (a) Experimental XRD pattern (black line) with the deconvolution (upper) and linear combination (lower) analyses for a 5 h sample from the 1:20 precursor to solvent series at 200 ^{o}C. Envelope patterns produced by each method are shown in green. Experimental XRD patterns of pure rh-In_2O_3 and bcc-In_2O_3 and NCs are shown in pink and blue, respectively. Bulk reference patterns for rh-In_2O_3, and bcc-In_2O_3 are shown by pink, and blue sticks, respectively. (b) Linear combination of rh-In_2O_3 and bcc-In_2O_3 EXAFS spectra to determine the phase content of a sample synthesized at 200 ^{o}C. (c) bcc-In_2O_3 fractional phase content as a function of time for samples synthesized using 1:20 precursor to solvent ratio at varying temperatures.

3.2 Kinetic Analysis of Phase Transformation

Equation 1.1 is employed to obtain the experimental *y* values for each sample at different points in time during the synthesis. The D_o and D_{rh} values were obtained from the peak broadening in the deconvolution analysis, and confirmed using TEM images of the corresponding NC population at a given point in time. The D_o values range between 2.0 and 3.5 nm, depending on reaction temperature. Using the ability to control NC interactions in solution phase by varying the starting precursor concentrations, this model-fitting approach was applied to examine the experimental data in the context of different mechanisms involving NC surfaces, particularly SN and IN. [37] This analysis allows for identification of the underlying phase transformation mechanism and determination of the associated parameters through fitting of the *y* data with different models. In this work, focus is placed on the surface-based mechanisms owing to the importance of high-energy sites in promoting the nucleation of a new phase.

The *y* values for samples of the 1:20 series synthesized at different temperatures are plotted as a function of time in Figure 3.3, together with the best fitting model for each temperature set, identified based on adjusted coefficient of determination (*R*-squared, R^2, Appendix A, Table A2) values and visual inspection. Figure 3.3a shows the *y* values for the lowest temperature in the series (200 ^oC); further decrease in the reaction temperature under the given conditions results in incomplete conversion of InOOH to rh-In_2O_3, and no phase transformation to bcc-In_2O_3 (Appendix A, Figure A1). The data in Figure 3.3a is best fit with eq 1.3.[96] With increasing temperature, the most appropriate model to describe phase transformation shifts systematically from SN to IN. The *y* data in Figure 3.3b is fit in two portions; data ranging from the starting point at 2 h through to 10 h were best fit with eq 1.2, while data ranging from 10 to 20 h with eq 1.3. With further increase in the reaction temperature (224 ^oC), the best fit is achieved with eq 1.2, indicating the dominant contribution from the IN mechanism (Figure 3.3c). This can be understood in the context of the NC contact probability, where higher temperatures lead to larger available kinetic energy and thus increased chances of NC collisions within the dilute suspension, favouring the IN mechanism. It should also be noted that fits were performed with an additional free parameter in the equations. This was done simply to prevent the function from being forced through the origin since these experimental data start at 2 h rather than 0 h,

which was the case in previous studies.[32,37] This delay is inherent to *in situ* phase transformation during colloidal synthesis in this work, as opposed to that of a pre-formed nanopowder phase.

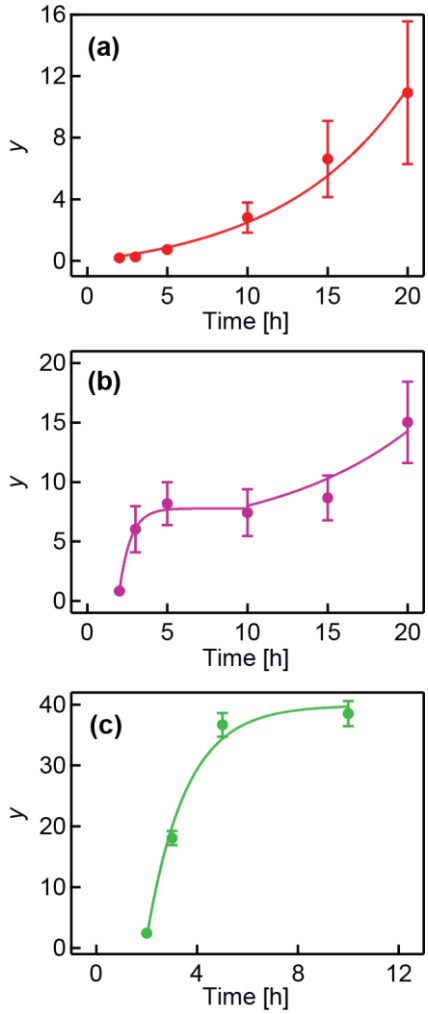

Figure 3.3: Kinetic data for phase transformation in samples synthesized with precursor to solvent ratio 1:20 at (a) 200 ^{o}C, (b) 211 ^{o}C, and (c) 224 ^{o}C. The solid lines are best fits to (a) y(SN), (b) y(IN)+y(SN), and (c) y(IN) models.

In addition to the 1:20 precursor to solvent ratio, samples were also synthesized with a 1:16 and a 1:12 ratio in order to directly compare the dilute and concentrated NC suspensions. The most notable difference between the two extreme series is the rate of phase transformation; while the 1:20 ratio 200 ^{o}C series required 20 h to reach 60 % conversion, the 1:12 series at nearly identical temperature (202 ^{o}C) reached 79 % conversion after only 6 h (Appendix A,

Figure A3). Additionally, the 1:20 series at 200 ^{o}C is a clear example of the SN mechanism, as evidenced by the fit with eq 1.3, whereas the 1:12 series at 202 ^{o}C is best modelled by the IN mechanism by fitting with eq 1.2 (Appendix A, Figure A4). This indicates that reduced particle contact probability in more dilute suspensions forces phase transformation to take place via the SN mechanism, which occurs at a significantly slower rate than the IN mechanism at the same temperature. These results demonstrate that it is possible to tune the mechanism and the degree of the phase conversion in the process of colloidal NC synthesis based on the precursor to solvent ratio and reaction temperature. By controlling these parameters, it has thus been demonstrated possible to completely separate SN and IN mechanisms, and achieve quantitative phase transformation by both mechanisms.

The kinetic parameters from fitting with the most appropriate models are summarized in Table 3.1 for all dilution series.[32,37] The rate constants generally increase with increasing temperature for both SN and IN. At low precursor concentration, the reaction is dominated by SN, and the contribution from IN is observed only at high reaction temperatures. The combined IN and SN behavior is also observed in the *y* vs *t* curves for intermediate dilution (1:16) reactions, but at lower temperatures (196 and 203 ^{o}C). The IN contribution appears minor but not necessarily negligible early on in the reaction, with the remainder being dominated by the exponential SN behavior.

Table 3.1: Mechanisms of Phase Transformation and Kinetic Parameters for Sample Series of Varying Dilution and Temperature

Dilution	T [^{o}C]	Model	k_{SN} [h^{-1}]	$k_{IN}N_o$ [h^{-1}]
1:20	200	y(SN)	0.1251	
	206	y(SN)	0.2145	
	215	y(IN+SN)	0.3359	1.086
	224	y(IN)		88.75
1:16	196	y(SN)	0.1410	
		y(IN+SN)	0.1327	0.0212
	203	y(SN)	0.2421	
		y(IN+SN)	0.2134	0.7044
	215	y(IN)		2.60
1:12	202	y(IN)		5.297
	212	y(IN)		10.29

Comparing the fits employed for different temperatures for a given dilution series, in particular the 1:20 series, reveals the systematic change in mechanism from SN to IN with increasing temperature and constant precursor to solvent ratio. This change illustrates that temperature provides another convenient avenue through which the mechanism can be controlled. These trends are summarized pictorially in Figure 3.4, which maps the dominant phase transformation mechanism observed for each dilution series (indicated with corresponding symbols) at different temperatures. As either temperature or precursor to solvent ratio is increased, the mechanism of phase transformation shifts from SN to IN, eventually becoming entirely IN. It should be noted that the phase transformation occurs in a surprisingly narrow temperature range, allowing for the acquisition of a relatively limited number of data points to model the phase transformation mechanisms. The results of this work thus suggest that through simultaneous control of temperature and precursor to solvent ratio, the mechanism of the nucleation of a new phase in the phase transformation process can be controlled in this colloidal NC system.

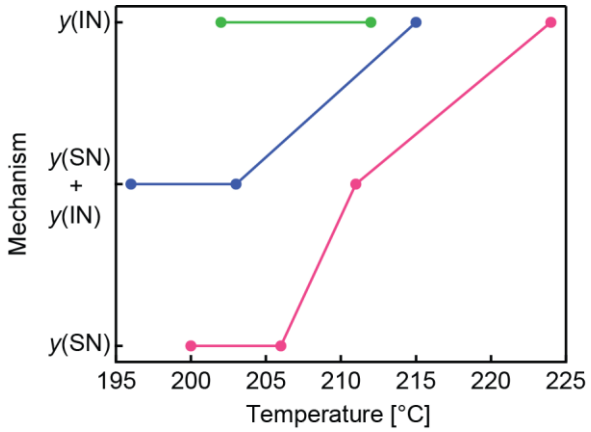

Figure 3.4: Mechanistic map showing the change in the mechanism of phase transformation through temperature and precursor to solvent ratio. Pink, blue, and green markers represent 1:20, 1:16, and 1:12 precursor to solvent ratios, respectively. Lines serve as a guide to the eye.

Figure 3.5 shows the Arrhenius plot constructed using the k_{SN} values from the 1:20 dilution series obtained at different temperatures. Using the Arrhenius expression (eq 1.6), these data were fitted and the activation energy, E_a, and pre-exponential factor, A_o, extracted. The activation energy for the SN process, E_a(SN), was determined to be ca. 124 kJ/mol, and A_o(SN) is 7.0×10^{12} h^{-1} (1.9×10^9 Hz).[97] The same analysis was performed for other dilutions (Appendix A, Figure A5), and the average E_a for SN was calculated to be 144±30 kJ/mol. This is an interesting and somewhat surprising result, since SN is expected to be a higher energy process than IN, for which E_a(IN) was determined to be ca. 150 kJ/mol in previous studies involving IN-driven phase transformation of colloidal In_2O_3 NCs,[32] and confirmed in this work.[97] Similar values of the activation energies are consistent with a very narrow temperature range in which the phase transformation occurs for this system. Unlike SN, which requires thermal fluctuations of atoms on rh-In_2O_3 NC surfaces to initiate the nucleation of a new phase, IN relies on the formation of cubic-like structure at the subset of rh-In_2O_3 NC interfaces to initiate the nucleation of the bcc-In_2O_3 phase. These results suggest that both processes may ultimately involve similar rearrangements of bonds. This is in contrast with anatase-to-rutile TiO_2 nanopowder phase transformation, for which E_a(SN) and E_a(IN) were found to be 466 and 167 kJ/mol,

respectively.[32,37] These results indicate not only that it is possible to manipulate *in situ* the mechanism of phase transformation during the synthesis of colloidal metal oxide NCs, but that the nucleation of a new phase is largely governed by local bonding rearrangement initiated by high-energy surface sites, rather than macroscopic properties of materials. Although SN and IN have similar activation energy, increasing temperature favors IN, as discussed above (Figures 3.3 and 3.4). This interesting and seemingly counterintuitive relationship is also different from that for TiO_2 nanopowder phase transformation, for which SN is found to dominate at higher temperatures. In colloidal suspensions, the probability of NC collision is based on Brownian motion, which also increases with temperature. In the kinetically-driven phase transformation in NC suspension, SN then may become a primary mechanism at low temperature not only because of the lower E_a, but also by reducing the NC interactions. These results indicate that the phase transformation of NCs during the colloidal synthesis is determined by different principles than the transformation of NCs in the powder form.

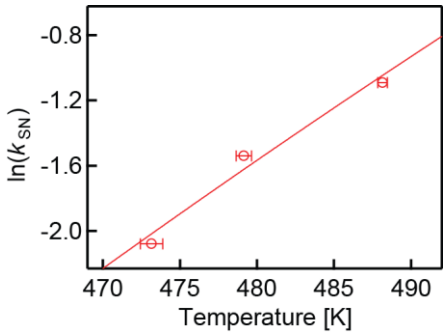

Figure 3.5: Arrhenius plot using the data from the most dilute series, 1:20, to obtain E_a(SN). The solid line is best fit to data points using eq 1.6.

3.3 Further Evidence of Coexisting Mechanisms

To provide a supporting evidence for phase transformation mechanisms under different conditions, high resolution TEM imaging and analysis was employed. Overview TEM images of NCs synthesized at 200 °C using 1:20 precursor to solvent ratio 5 h after the final reaction temperature had been reached are shown in Appendix A, Figure A6. Most NCs exhibit nearly spherical shape, although there are a few displaying elliptical or dumbbell morphology. Figure

3.6a shows a typical image of a single rh-In_2O_3 NC from this sample. The NC appears to have quasi spherical or rectangular shape, measuring ca. 4.3 nm in diagonal direction. The measured lattice spacing of 2.87 Å corresponds to the {104} lattice plane of rh-In_2O_3. The same sample contains both rh- and bcc-In_2O_3 phase, as evident from the corresponding XRD data in Figure 3.1. The critical NC size for phase transformation from rh- to bcc-In_2O_3 is ca. 5 nm, as examined in greater detail in previous works.[8,32]. Somewhat larger NCs with very similar morphology and lattice spacing of 2.91 Å corresponding to the {222} planes of bcc-In_2O_3 were also observed (Figure 3.6b), suggesting that phase transformation spontaneously occurs by SN once NCs attain the critical size. Although rh-In_2O_3 {104} and bcc-In_2O_3 {222} planes have similar lattice spacing, virtually all NCs smaller than the critical size exhibit an electron diffraction pattern characteristic for rh-In_2O_3.[10] Similar observations were made at shorter reaction times, consistent with the kinetic analysis in Figure 3.3a, indicating the dominant SN mechanism even early on in the reaction under these conditions (Appendix A, Figure A7). However, increasing precursor to solvent ratio results in a dominant population of larger NCs that have irregular shapes derived by two joined NCs (Appendix A, Figures A8, A9). Figure 3.6c depicts two NCs joined via oriented attachment, with 4.12 Å lattice spacing also indicating bcc-In_2O_3 phase ({211} plane). This observation is consistent with the phase transformation initiated by IN at the particle-particle contact point. As expected, not all NC contact formation leads to the phase transformation. Figure 3.6d shows an example of two rh-In_2O_3 NCs joined by oriented attachment, while retaining the corundum crystal structure. The interface between two NCs contains no observable dislocations or defects which could form in oriented NC attachment,[98] and are suggested to be necessary for phase transformation by IN.[99-101] The lack of interfacial defects is consistent with the retention of rh-In_2O_3 phase upon NC attachment. Importantly, all NCs examined by TEM consist only of a single phase. This observation is consistent with a very rapid single-step transformation once the new phase nucleates on the NC surfaces or interfaces. Taken together, the results of Figure 3.6 demonstrate that both IN and SN mechanisms will simultaneously play a role in phase transformation kinetics of colloidal NCs.

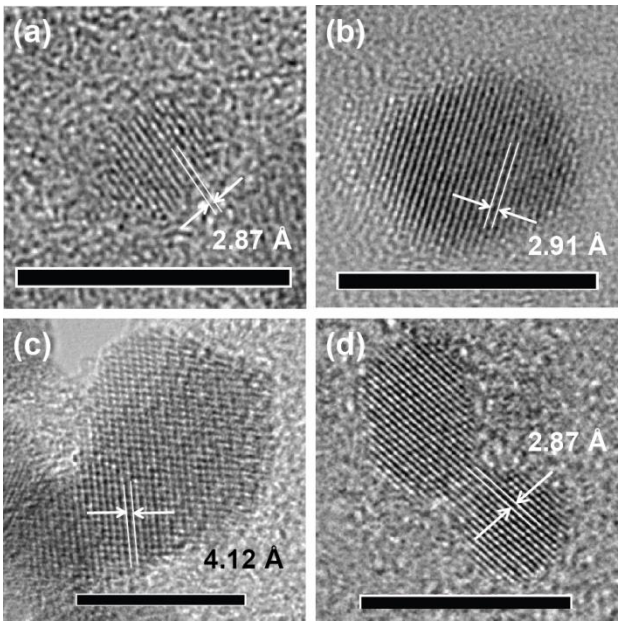

Figure 3.6: Typical lattice-resolved TEM images of individual NCs in the course of the colloidal synthesis. (a,b) NCs obtained after 5 h at 200 ^{o}C: (a) rh-In_2O_3 NC identified by the {104} plane, and (b) bcc-In_2O_3 NC identified by the {222} plane, illustrating the possibility of phase transformation via SN mechanism. (c) NCs obtained after 20 h at 200 ^{o}C. NCs having bcc-In_2O_3 structure identified by {211} plane are joined by oriented attachment, demonstrating that phase transformation may also occur by IN mechanism. (d) Oriented-attached rh-In_2O_3 NCs showing no phase transformation upon contact formation. The lack of mixed-phase NCs illustrates that the transformation is rapid once the bcc phase has been nucleated. Scale bars in all images, 10 nm.

Taken together, the results of this work are summarized pictorially in Figure 3.7. Figure 3.7a and b illustrates the effect of precursor concentration and reaction time on the phase transformation mechanism, using pink (rh-In_2O_3 NCs) and blue (bcc-In_2O_3 NCs) spheres. High NC concentration leads to high probability of contact formation and IN (Figure 3.7a), while SN is more likely to occur in diluted suspensions and requires longer time for the completion of phase transformation (Figure 3.7b). The formation of nucleation sites at NC contact points in IN is contrasted with the SN mechanism in which the nucleation site forms on the surface of a lone

NC as it grows. Additionally, rh-In_2O_3 NCs can fuse by oriented attachment without undergoing phase transformation, if the joining NCs are sufficiently small and contain no defects at the contact points, as depicted in Figure 3.7a. The role of the probability of NC contact formation for the mechanism of phase transformation is confirmed by comparing the reaction yield of the samples prepared using 1:12 and 1:20 precursor to solvent ratio at 200 °C, for the durations that result in similar NC sizes (Appendix A, Figure A10). The yield of the reaction for 1:12 dilution is ca. 25 % higher than that for 1:20 sample, indicating overall significantly higher concentration of NCs for 1:12 sample. Furthermore, a larger number of elongated (oblong or dumbbell-shaped) NCs is observed for the 1:12 sample, also consistent with IN mechanism. Figure 3.7c and d shows the impact of temperature on the phase transformation mechanism. Elevated temperatures lead to an enhancement in NC collisions and thus phase transformation by IN (Figure 3.7c). At low temperatures, slower Brownian motion decreases the rate of NC contact formation and favors SN (Figure 3.7d). Understanding the influence of these variables allows for the control of the mechanism at work and the rate of the colloidal NC phase transformation process.

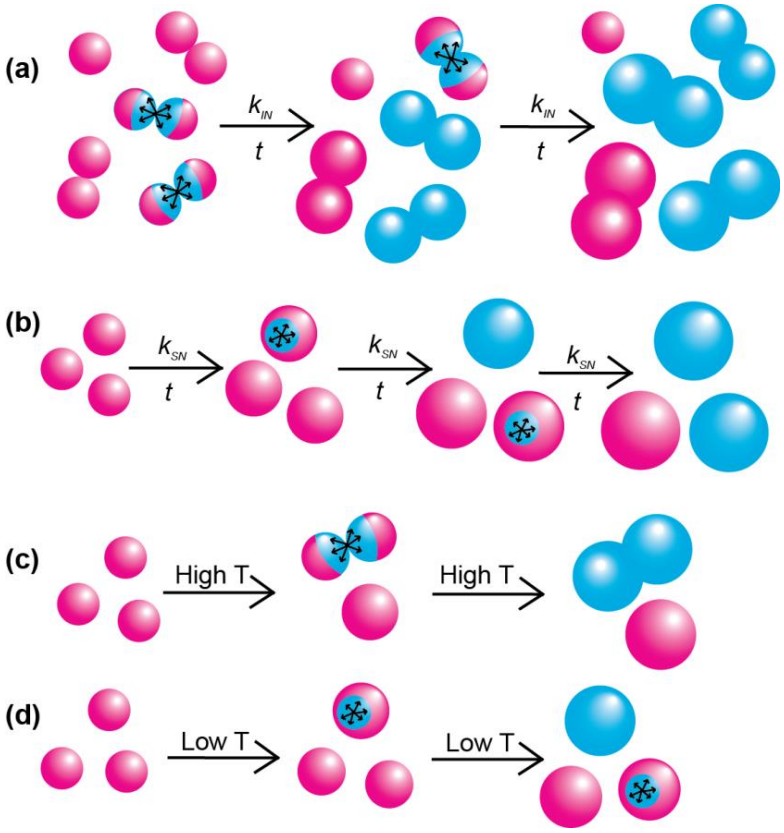

Figure 3.7: (a,b) Illustration of (a) IN and (b) SN phase transformation mechanisms through manipulation of the precursor to solvent ratio and allotted reaction time. (c,d) Illustration of temperature impact on the mechanism, where higher temperatures lead to IN (c) and lower temperatures allow for SN (d), respectively. Pink and blue spheres represent rh-In_2O_3 and bcc-In_2O_3 NCs, respectively.

Chapter 4 – Fundamental Characterization of Iron Doped Indium Oxide Nanocrystals

4.1 Influence of Iron Dopant on Nanocrystal Structure and Morphology

Comparison of undoped and doped In_2O_3 NCs synthesized under identical conditions reveals the influence of Fe dopant on the observed NC phase (Figure 4.1a). The internal synthesis temperatures were 212 ^oC for pure In_2O_3 and 211 ^oC for Fe-doped In_2O_3, and thus temperature can be considered constant. In both cases, the precursor to solvent ratio was 1:12 and the reaction was allowed to continue for 1 h. There is a stark contrast between the 52% bcc-In_2O_3 NCs and the 94% rh Fe-doped NCs, indicating that the dopant is responsible for the continued presence of the rh phase. Considering the size-phase relationship of In_2O_3, it can be speculated that NC growth was sufficiently hindered by the combination of Fe dopant and low temperature conditions to maintain NC sizes ≤ 5 nm and thus facilitate retention of the rh phase.

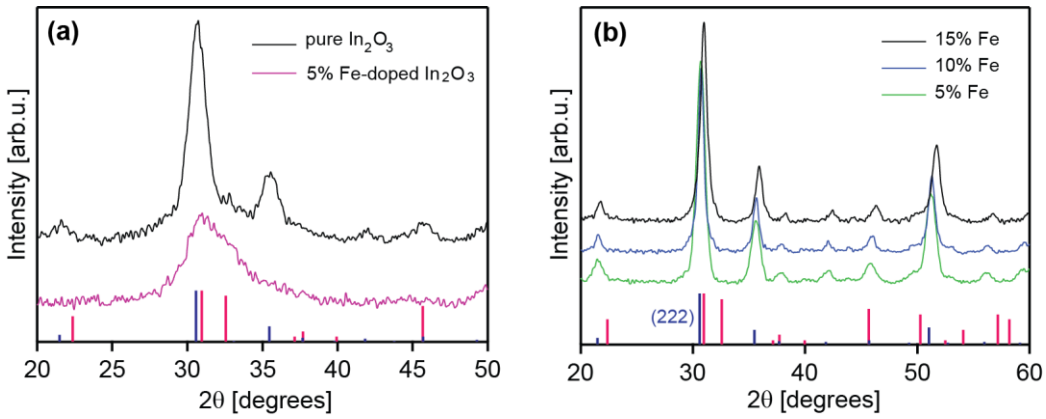

Figure 4.1: (a) XRD patterns of pure and Fe-doped In_2O_3 NCs, black and pink lines, respectively, synthesized under identical conditions. The pure In_2O_3 is a nearly 50-50 mixture of bcc and rh phases, while the Fe-doped NCs are 94% rh phase. (b) XRD patterns illustrating the effects of doping concentration on phase. With a constant high temperature and increasing doping concentration, bcc phase NCs are obtained and a subtle shift in the (222) reflection towards higher 2θ is observed. Pink and blue sticks indicate rh-In_2O_3 and bcc-In_2O_3 reference patterns, respectively.

With higher temperature synthesis, internally ca. 230 ^{o}C, all samples contain only bcc-In_2O_3 NCs, regardless of doping concentration (Figure 4.1b). This implies that higher temperatures provide sufficient energy to promote NC growth beyond the critical size despite any impedance due to the dopant. Interestingly, however, it was found that higher doping concentrations (i.e., 10% and 15%) at slightly lower temperatures also resulted in bcc phase NCs. This suggests that the combination of low doping concentration (5%) and low temperature (210 ^{o}C) results in stabilization of the rh phase, while a relatively small increase in either parameter rapidly leads to bcc phase NCs. This is unexpected for a few reasons. Firstly, the most stable phase of Fe_2O_3 is hematite, α-Fe_2O_3, which has a rhombohedral corundum type structure.[82,83] Thus, it would be anticipated that rh-In_2O_3 would be the favoured host lattice when Fe dopant is present due to the structural similarity between the two materials.[102] Moreover, β-Fe_2O_3, which has cubic bixbyite structure, is the least common phase of Fe_2O_3 due to its thermodynamic instability,[82] and so it is unexpected that Fe would favour a cubic bixbyite host. Secondly, stabilization of the rh phase was observed in Cr and Mn-doped In_2O_3 systems as the population of NCs below the critical size increased with increasing doping concentration as a result of NC growth inhibition, leading to smaller populations of bcc phase NCs.[9] Thus based on XRD patterns alone, Fe as a dopant can already be identified as behaving opposite to that observed previously with Cr- and Mn-doped In_2O_3 systems, prompting further experimental investigation.

In order to provide further insight into the relationship between NC phase, size, doping concentration, and internal synthesis temperature, the particle sizes of several bcc phase samples were estimated using the Scherrer equation (eq 2.1). TEM imaging was also employed to aid in this evaluation. Table 4.1 summarizes the particle sizes obtained by the Scherrer equation and 2θ values at which the bcc (222) reflection is centred for each sample.

Table 4.1: Parameters Extracted from XRD Patterns of Fe-doped bcc-In_2O_3 Samples

T [^{o}C]	mol% Fe	Particle Size [nm]	2θ of the (222) Reflection
210	10	6.69	31.0
	15	7.85	31.0
220	10	7.09	30.9
	15	9.84	31.0
230	5	8.86	30.7
	10	12.4	30.7
	15	10.4	31.0

The 2θ value of each (222) reflection shifts to marginally higher values with increasing doping concentration, possibly suggesting a shrinking of the lattice with increased Fe incorporation. It can be seen that the calculated particle size generally increases with increasing doping concentration and temperature, the sizes ranging overall from ca. 6 to 12 nm. Considering an increase in either parameter, the particle growth is not dramatic; this indicates that changing the temperature or doping concentration has a small impact on particle size once the bcc phase is achieved.

Comparison of the Scherrer equation estimated particle sizes with corresponding particle size distributions obtained via TEM imaging reveals that the bcc particle diameters are ca. 1 nm smaller than that indicated by XRD. The particle size distributions shown in Figure 4.2 are somewhat broad, and bimodal size distributions as was observed for Cr and Mn doped samples are not as obvious in this case.[9] Figure 4.2a shows that at 5% doping concentration and increasing temperature, the largest population of NCs shifts from 3 to 9.5 nm sized particles; this corresponds to the anticipated change in phase from rh to bcc, as indicated by XRD. The broadest distribution of particle sizes is observed at the medium temperature, 220 ^{o}C, in this case. In Figure 4.2b, where temperature is held constant and the doping concentration is increased, it can be seen that the largest NC population does shift slightly to larger size as the doping concentration is increased, but more notably the size distribution broadens with increasing doping concentration. These results suggest that increasing synthesis temperature causes a more

uniform increase in particle size than does increasing the doping concentration, though increasing either parameter ultimately results in a particle size increase. This again contrasts with previous studies on Mn doped In_2O_3, where NC sizes decreased systematically with increasing doping concentration.[9] It should be noted that TEM images utilized for particle sizing were nearly all high resolution.

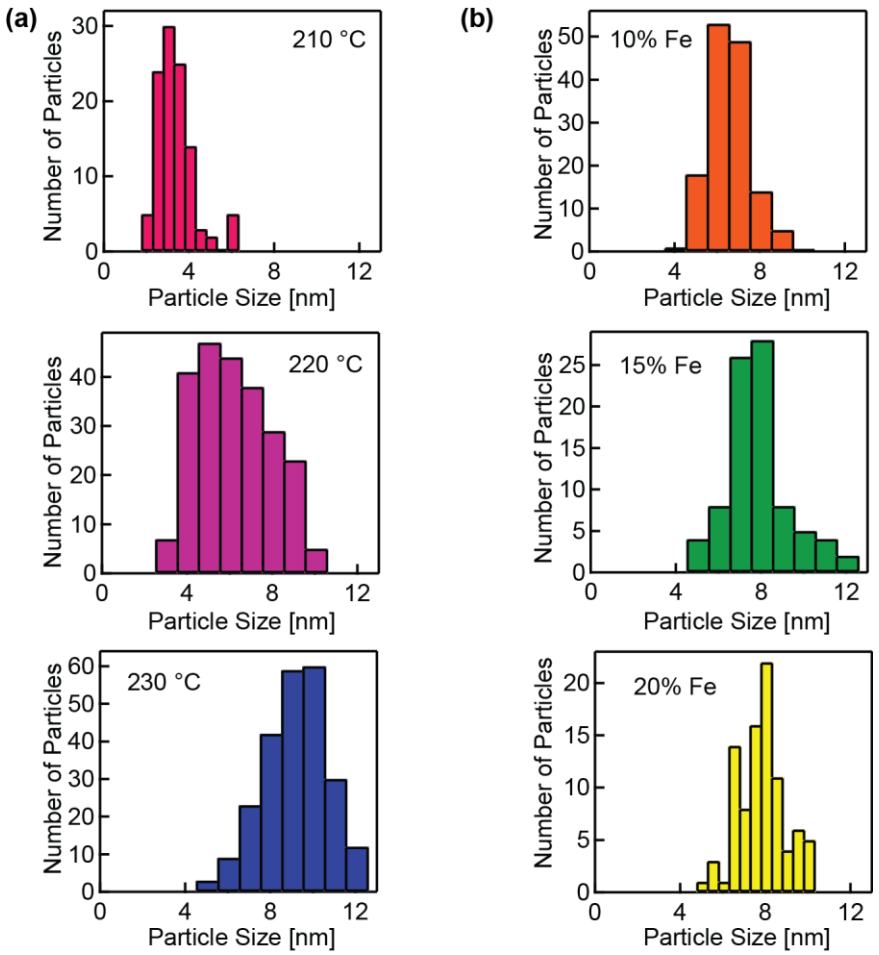

Figure 4.2: Particle size distributions obtained via TEM images for (a) constant 5% Fe doping concentration with varying synthesis temperature from 210 to 230 ^{o}C, and (b) constant 220 ^{o}C synthesis temperature with varying Fe doping concentration from 10 to 20%.

Further examination of HR-TEM images confirms the phase-size relationship of the doped NCs via measurement of the lattice spacings. NCs synthesized with 5% Fe dopant at temperatures of 210 ^{o}C and 230 ^{o}C are shown in Figure 4.3a,b, respectively, demonstrating the presence of rh and bcc NCs in the low and high temperature regimes, respectively. The lattice spacing determined for the NC shown in Figure 4.3a corresponds to that of rh-In_2O_3, 2.87 Å, with a particle diameter of 3.8 nm, much smaller than the critical size for phase transformation. By contrast, the NC in Figure 4.3b has lattice spacing 2.93 Å, corresponding to bcc-In_2O_3, and the particle diameter is 11.2 nm.

TEM imaging additionally reveals the tendency towards NC self-assembly and the formation of relatively large nanoflower structures in this system. Figure 4.3c,e depict nanoflowers identified in samples synthesized with 10 and 20% Fe, respectively, with high temperature syntheses in both cases; Figure 4.3d,f show the corresponding nanoflower size distributions. It can be seen that increasing the doping concentration from 10 to 20 % results in an increase in the largest nanoflower population size from 35 to 40 nm. Regardless of whether the synthesis temperature was high or low, nanoflower formation was only observed when the doping concentration was greater than 5%; nanoflowers did not form in 5% Fe samples. Similar NC self-assembly was observed in the case of Mn-doped In_2O_3 NCs, where the use of $MnCl_2$ precursor at relatively high doping concentrations resulted in nanoflower formation.[70] In that particular study, nanoflower formation was correlated with increased ionic strength of the solution during synthesis; adsorption of Cl^- from the $MnCl_2$ precursor onto the NC surfaces resulted in unequal charging of the surfaces and thus possible local dipole moment formation, which would lead to the necessary attractive interactions between nearby NCs for self-assembly.[70] Since the precursor employed in synthesis of Fe-doped In_2O_3 NCs was $FeCl_3$, the presence of Cl^- is again implicated as the driving force behind nanoflower formation. Consequently, the lack of nanoflowers at 5% Fe can be associated with insufficient Cl^- anions to induce enough of a surface charge that would lead to nanoflower assembly.

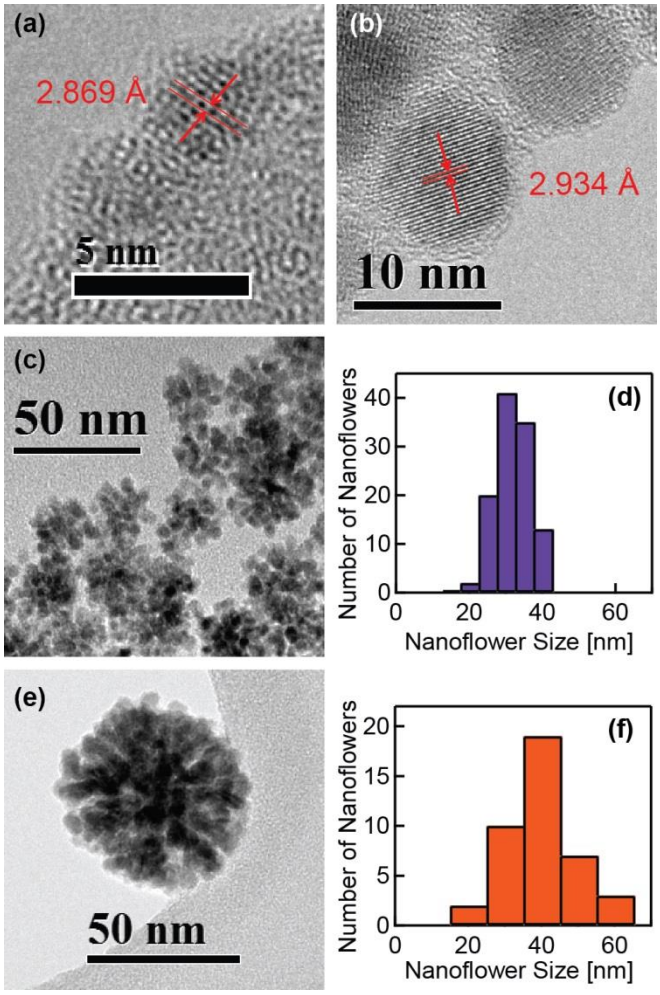

Figure 4.3: (a,b) HR-TEM images of Fe-doped In_2O_3 NCs synthesized at (a) 5% Fe, 210 ^oC and (b) 5% Fe, 230 ^oC, identified as rh and bcc phase, respectively, based on the corresponding measured lattice spacings of 2.87 and 2.93 Å. (c,d,e,f) Nanoflower formation and size distributions are shown for high temperature syntheses (230 ^oC) with (c,d) 10% and (e,f) 20% Fe-dopant.

At this point, further structural analysis utilizing spectroscopic techniques in addition to magnetization measurements are essential in order to better understand this TM-doped colloidal NC system. A subset of the samples discussed in this section will be focused on in an effort to obtain the most revealing data. Assessment of the actual amount of Fe incorporated into the NC host is also of great importance given that it will directly influence conclusions drawn from all characterization methods.

4.2 Intended and Actual Doping Concentrations

The amount of dopant that is actually incorporated into the host lattice is often different from the intended doping concentration during synthesis, a consequence of how easily the dopant is incorporated into the host under given conditions. This consideration is of great importance when assessing physical properties such as the saturation magnetization, which are directly related to the true amount of dopant present. ICP-AES analysis was used to determine the actual concentration of Fe atoms incorporated into the NCs, the results of which are summarized in Table 4.2.

Table 4.2: Actual Doping Concentration as Determined by ICP-AES

Initial mol%Fe	T [^{o}C]	Phase	Actual mol%Fe
5%	210	rh	1.26%
5%	230	bcc	1.77%
10%			5.57%
15%			7.87%

In each case, the actual percentage of Fe is significantly lower than the intended doping concentration. This is contrary to many reports in which Fe is quite soluble in the In_2O_3 lattice.[20,79,103] Previous studies involving Fe-doped In_2O_3 synthesized via solution techniques have reported actual doping concentrations very similar to those of the intended doping concentration; however, they do not report use of a capping agent such as TOPO.[79,80,104] This

suggests that many dopant ions are surface bound, and the actual amount incorporated within the host lattice is significantly smaller than intended. Despite the overall low percentages of Fe, it can be seen that as the doping concentration is increased, the relative percentage incorporated also increases; about one-quarter of the 5% initial dopant amount is actually incorporated, while just over half of the 10 and 15% dopant is integrated into the host lattice. This is not unlike the trend observed in the case of Cr-doped In_2O_3, the major difference being that the fraction of rh phase increased with increasing Cr doping concentration, thereby indicating a higher solubility of Cr in the rh lattice.[9] Conversely, Mn-doped In_2O_3 displayed trends opposite to that of Cr, preferring the bcc phase as the actual doping concentration decreased with increasing rh fraction.[9] Thus in this case, these trends suggest Fe is more soluble in the bcc phase than in the rh phase. However, it is also worth noting that the percentage of Fe incorporated into the 5% rh and 5% bcc phase samples is still very similar, the actual amount of Fe in the bcc phase being greater by only ca. 0.5%. This implies that temperature has a stronger influence on the observed phase via NC growth kinetics than does the intended doping concentration, and thus the Fe dopant is nearly equally soluble in either bcc or rh phase NCs. If this were not the case, it would be anticipated that one phase would have a notably higher percentage of incorporated Fe despite the same initial doping concentrations. As previously stated, literature indicates that Fe should be very soluble in In_2O_3 lattice; these studies refer to bcc-In_2O_3, yet reports have also suggested that the small size of Fe^{3+} compared to In^{3+} make it an ideal candidate for stabilization of the rh phase.[102] Taken together, these findings may suggest that the Fe-dopant is nearly equally soluble in both phases of the In_2O_3 host, with a slight preference for the bcc phase. This then further supports the observation of bcc NCs at high doping concentration where studies with other TM dopants indicate a trend towards small rh NCs under such conditions.

It should be noted that going into further analysis, samples will still be referred to by their nominal doping concentrations as opposed to the actual values. The starting concentration of dopant is indeed the most important factor for NC growth inhibition in these studies, and thus it is of importance to keep these values in mind. However, in calculations of magnetization per dopant atom, the actual doping concentrations are taken into account.

4.3 Spectroscopic Studies

Spectroscopic techniques can yield information regarding the structural environment of a material in addition to revealing details of the electronic structure. In order to examine the local environment surrounding the Fe dopant, establish the oxidation state of Fe, and confirm the absence of secondary phases in the samples, X-ray absorption spectroscopy (XAS) was employed. Fe K-edge spectra were analyzed in the X-ray absorption near edge structure (XANES) region for samples of varying temperature, phase, and doping concentration. Absorbance in the ultraviolet-visible (UV-vis) region was also measured in order to examine shifts in the band gap and identify any transitions arising due to the Fe dopant.

4.3.1 X-ray Absorption Spectroscopy: XANES Analysis

In addition to identification of the K-edge energy, XANES analysis of TM absorbers typically involves examination of characteristic pre-edge features as they are indicative of the local site symmetry and orbital occupancy.[105] In the case of first row TM ions, the pre-edge feature is the result of 1s → 3d electronic transitions, the intensity of which increases with the breaking of inversion symmetry.[105,106] The 1s → 3d transition is formally dipole forbidden; however, mixing of 3d and 4p states results in the reduction in symmetry which enables this transition to gain intensity.[106,107] Alternatively, the pre-edge feature may result from 1s → 3d quadrupole transitions.[94,106,107] The centroid, or intensity-weighted average of the pre-edge component energy positions[94], is correlated with the oxidation state of the TM absorber, a higher energy centroid indicating a higher oxidation state.[94] It should be noted, however, that the coordination number of Fe also influences the pre-edge and therefore must be considered when estimating the contribution of different redox states to the material.[94] For the Fe K-edge in particular, it has been shown that though several portions of the XANES spectra may be used to quantify relative amounts of Fe oxidation states, fitting of the pre-edge feature and subsequent analysis of the centroid proves to be the most consistent with other established techniques, such as Mössbauer spectroscopy and wet chemical methods.[94,107] Many additional studies have shown that for systems containing Fe, ranging from minerals to Fe-doped In_2O_3 nanostructured materials, such evaluation of the XANES pre-edge feature is an effective strategy for obtaining symmetry and oxidation state information.[94,95,106,108-111]

Figure 4.4a plots XANES spectra of the reference materials hematite (Fe_2O_3) and olivine ($(Mg^{2+}, Fe^{2+})_2SiO_4$), which represent Fe^{3+} and Fe^{2+} oxidation states, respectively. Both hematite and olivine contain Fe in 6-coordinate sites with octahedral symmetry (O_h).[94] In Figure 4.4b, XANES spectra of Fe-doped In_2O_3 NC samples of varying doping concentration and synthesis temperature are shown. In both figures, the pre-edge feature is expanded in an inset plot. It can be seen that the reference materials of differing oxidation state have very distinctive spectra, whereas those of the Fe-doped In_2O_3 samples are similar amongst themselves, yet different from the references. This is a good indication that an Fe_2O_3 secondary phase is not present in the samples; for extra confirmation, however, spectra for additional standards such as iron(II) oxide (FeO) and magnetite (Fe_2O_3) should be collected in the future. The absence of secondary phases may also be confirmed via analysis of the extended X-ray absorption fine structure (EXAFS) region; EXAFS analysis remains a task for future studies as additional scans of this spectral region are required. Closer examination of the sample pre-edge features in the inset of Figure 4.4b reveals that the intensity of the 5% Fe, 210 ^oC pre-edge, which is the only rh phase material, appears to be greater than that of the bcc phase samples, in addition to having a different shape. This suggests that the rh lattice in this case has a larger amount of disorder surrounding the Fe atoms than does the bcc lattice, leading to increased pre-edge intensity, as well as suggesting a potentially different mixture of Fe oxidation states. It is assumed that Fe remains 6-coordinate in the In_2O_3 lattice for both the bcc and rh phases; the presence of oxygen vacancies could in reality result in lower coordination, which would have an influence on the pre-edge feature. Exact coordination numbers can be confirmed through EXAFS analysis.

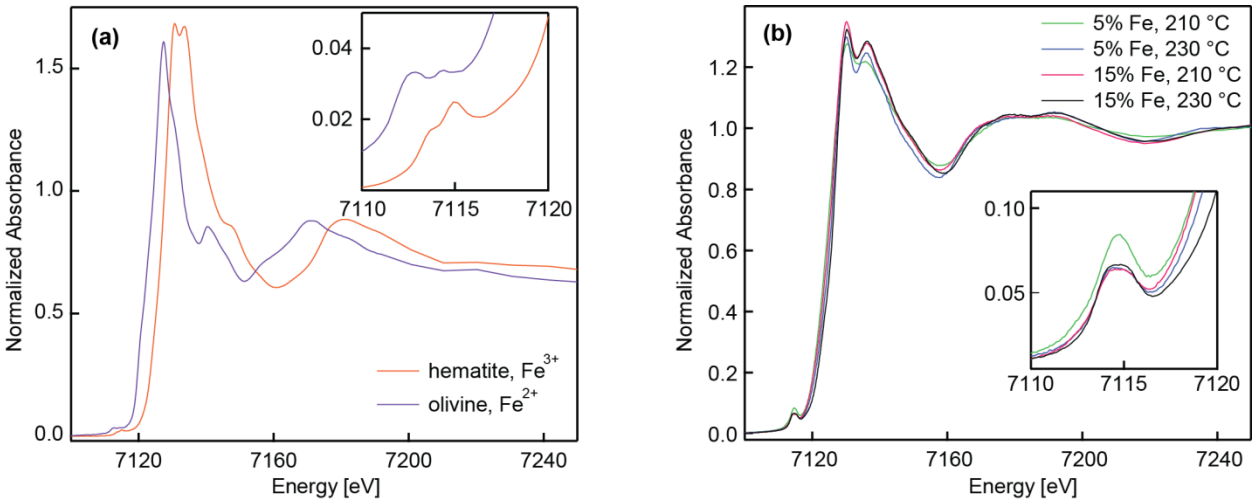

Figure 4.4: XANES spectra of (a) reference materials hematite (orange) and olivine (purple), corresponding to Fe^{3+} and Fe^{2+}, respectively, and (b) Fe-doped In_2O_3 samples of varying doping concentration and synthesis temperature. Insets show expanded plots of the pre-edge features.

Select results from the pre-edge fitting analysis are shown in Figure 4.5. According to Wilke *et al.*, 6-coordinate Fe^{2+} is fit with three peaks based on theoretical predictions, while Fe^{3+} in a 6-coordinate environment is fit with two peaks.[94] This is clearly demonstrated in Figure 4.5a,b as hematite is best fit with two peaks and olivine with three. Fitting of the Fe-doped In_2O_3 samples with two peaks resulted in the best fit, preliminarily suggesting that Fe is indeed in an octahedral coordination and that Fe^{3+} is either the predominant or only oxidation state of Fe present (Figure 4.5c,d). From these fittings, the individual peak energy locations are used to calculate the centroid, and the integrated area of each peak is summed to give the total area of the pre-edge feature. All fitting results are summarized in Appendix B, Table B1, and the centroid calculation is demonstrated in Appendix B. The standard error associated with fitting is on the order of ±0.001 for all samples, and the associated R^2 values are listed in Table B1.

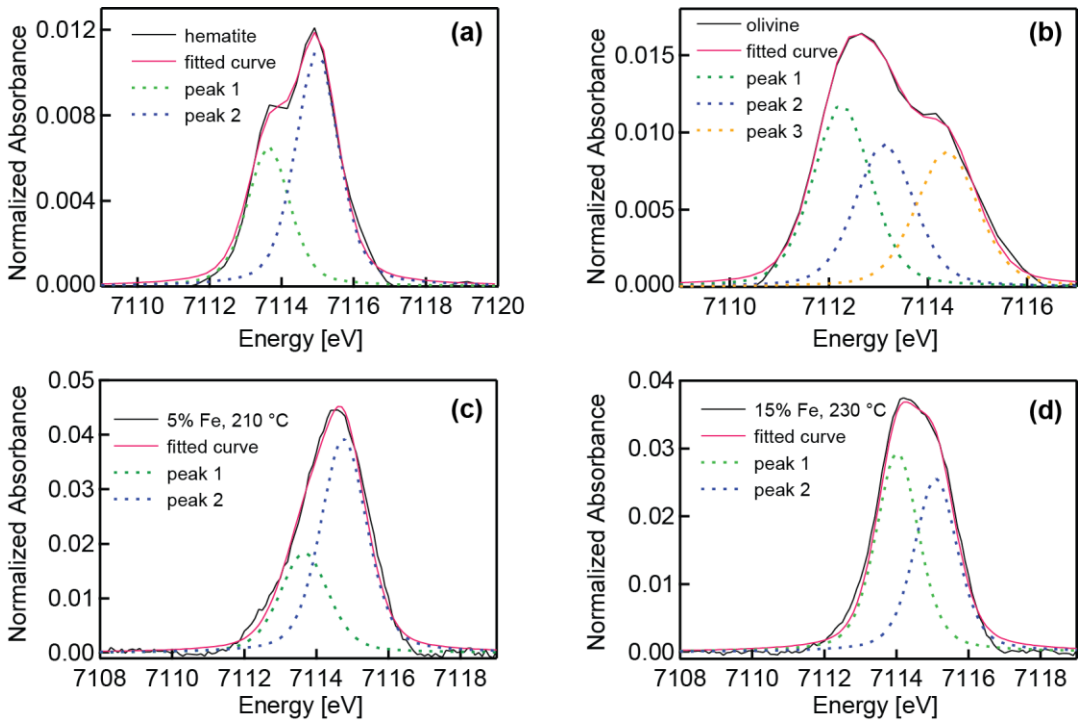

Figure 4.5: XANES pre-edge feature analysis of (a,b) reference materials and (c,d) Fe-doped In_2O_3 NC samples. In all plots, black and pink solid curves indicate the experimental and fitted spectra, respectively. Green, blue, and yellow dashed curves indicate the 50:50 Gaussian-Lorentzian peaks which convolute to generate the fitted curve. (a,b) Minerals (a) hematite and (b) olivine serve as the Fe^{3+} and Fe^{2+} references, respectively. (c,d) Fe-doped In_2O_3 NC samples are (c) 5% Fe, rh phase at 210 ^oC and (d) 15% Fe, bcc phase at 230 ^oC.

As a visual summary of the pre-edge fitting results, plotted below in Figure 4.6a are the total areas as a function of the centroid energy position. Using the hematite and olivine standards as indicators of the Fe^{3+} and Fe^{2+} oxidation states, it can immediately be seen that the centroid positions of the Fe-doped samples are very close to that of hematite. This indicates that the majority of doped Fe is indeed Fe^{3+}; however, the deviations from the Fe^{3+} location suggest Fe^{2+} may also be present. It has been shown that maintaining a constant coordination and varying the oxidation state, or vice versa, the centroid position varies linearly with oxidation state.[107] Thus, using the hematite and olivine centroid references of known oxidation state and assuming all Fe atoms in the samples are 6-coordinate, the $Fe^{3+}/\Sigma Fe$ ratios in the samples were estimated (Figure

4.6b). Of all samples, only 15% Fe synthesized at 230 °C was identified as being entirely Fe^{3+}; the other three samples were estimated to contain ca. 90% Fe^{3+} and 10% Fe^{2+} (Appendix B, Table B2). This suggests that similarly to the Mn-doped system[70], a redox process occurs during synthesis which results in reduction of Fe^{3+} to Fe^{2+}. Additional evidence supporting the presence of mixed valence Fe can be seen in the energy location of the absorption edges (Appendix B, Table B3); in all cases, the absorption edges of the nanocrystalline samples are between those of the references hematite and olivine, an indication that Fe^{2+} and Fe^{3+} are both present. To confirm the specific $Fe^{3+}/\Sigma Fe$ ratios established here, a technique such as Mössbauer spectroscopy should be employed in the future.

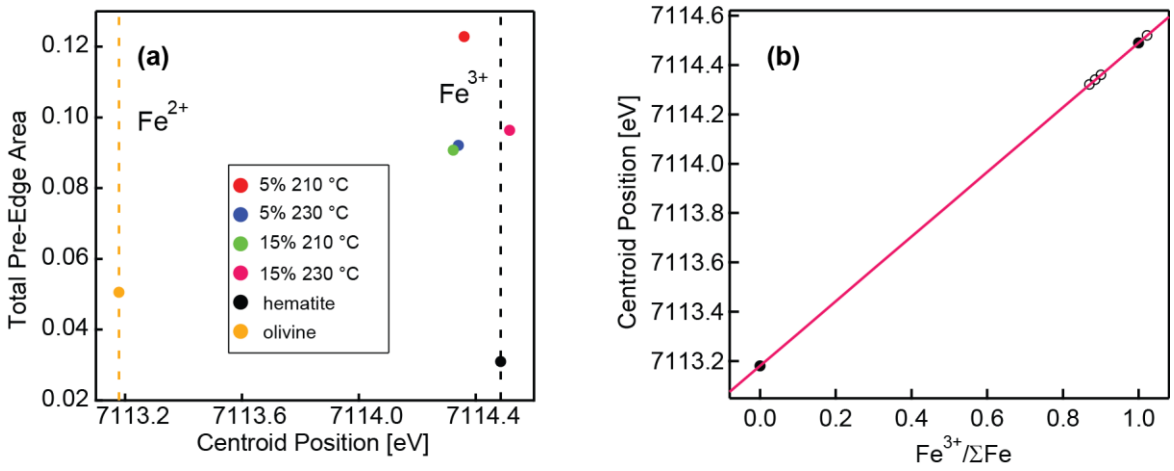

Figure 4.6: (a) Total pre-edge area as a function of the centroid position established from fitting of the Fe-doped In_2O_3 and reference materials pre-edges. Dashed yellow and black vertical lines serve as a guide to the eye for the Fe^{2+} and Fe^{3+} references, respectively. (b) Using the known oxidation states and centroid positions of the references hematite and olivine (filled circles) to estimate the ratios of Fe^{3+} and Fe^{2+} in the Fe-doped In_2O_3 samples (open circles). The pink calibration line was generated using the two reference points.

Quantitative pre-edge analysis confirmed that the 5% Fe, 210 °C sample with rh phase does indeed have a slightly greater pre-edge total area than that of the bcc samples. This implies

that the dopant incorporation sites are more highly distorted in the rh phase. Assuming that Fe is substitutionally incorporated and thus in a 6-coordinate environment in all cases, this observation may allude to the specific sites in which Fe resides within the bcc lattice. The rh lattice contains only one type of In site, in which the oxygen atoms are arranged in a trigonal antiprism about In[25], and the symmetry of these sites is C_{3v}.[9] For the two possible locations within the bcc phase, the b-sites are of D_{3d} symmetry[9] and the d-sites are highly distorted with C_2 symmetry.[112] Since Fe must be incorporated into the C_{3v} sites of the rh lattice and the pre-edge data indicates that this is the most disordered sample, it is reasonable to presume that Fe incorporates into the b-sites of the bcc phase samples, which are of higher symmetry and thus more highly ordered. If Fe were incorporated into the d-sites, it would be expected that the pre-edge total area of the bcc samples would be greater than that of the rh sample since the symmetry is lower and thus the disorder would be higher. It is important to note, however, that this particular discussion has been purely speculative in nature; the larger surface to volume ratio of the rh phase could be the source of additional distortion as opposed to the rh structure itself. Dopant site occupation will need to be confirmed through EXAFS analysis, where the bond lengths can be used to identify specific incorporation sites as well as determine the exact coordination number.

4.3.2 UV-vis Absorption Spectroscopy: Electronic Structure

In order to obtain basic information regarding the electronic structure and optical properties, UV-vis absorption spectra were collected for several Fe-doped samples. Figure 4.7a displays the spectra of four key samples. As demonstrated in previous works[8], the band gap transition in In_2O_3 NCs appears as a broad shoulder in the region of ca. 260 to 340 nm. Using first derivative plots of the spectra, the band gaps were identified and the results are summarized in Table 4.3. Knowing that the band gap of bulk In_2O_3 is ca. 3.75 eV, it is evident from the relatively large band gap energies that all NCs experience quantum confinement, the rh sample being the most confined, as would be anticipated since these NCs are the smallest.

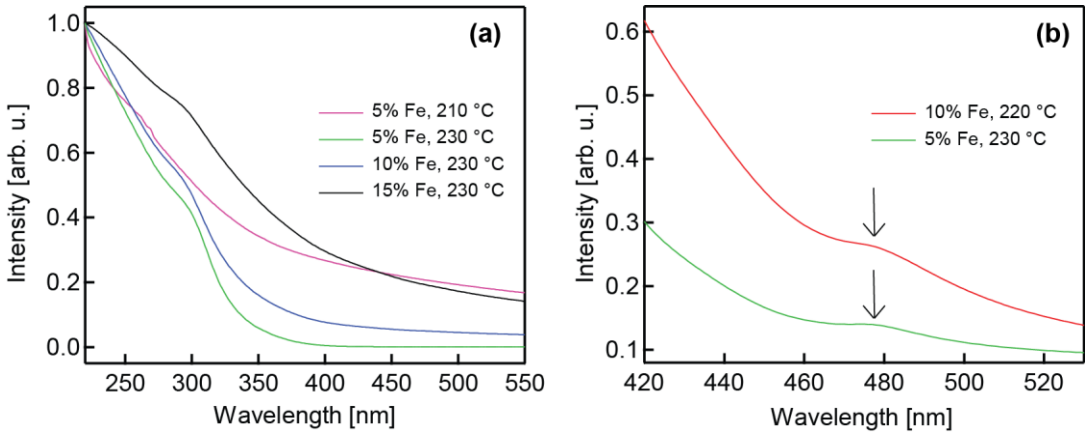

Figure 4.7: UV-vis absorption spectra of samples (a) varying in doping concentration and synthesis temperature. (b) Demonstration of charge transfer absorption peak observed in spectra of very concentrated samples. All spectra were collected in hexane and have been normalized.

Table 4.3: Band Gaps of Fe-doped In_2O_3 NCs as Determined by UV-vis Spectroscopy

Doping Concentration	Phase	T [^oC]	Band Gap [nm]	Band Gap [eV]
5% Fe	rh	210	271	4.56
	bcc	230	312	3.96
10% Fe	bcc	230	309	4.00
15% Fe	bcc	230	309	4.00

Aside from the band gap, the spectra contain no obvious additional features. However, collecting the absorption spectra of relatively concentrated colloidal solutions reveals a weak transition at ca. 478 nm (Figure 4.7b). Considering that Fe is mostly Fe(III) with a small contribution from Fe(II), this peak is likely the result of either a crystal field *d-d* transition or a charge transfer transition.[113] Since 6-coordinate Fe(III) is a somewhat oxidizing species, it is known to readily undergo ligand to metal charge transfer (LMCT) transitions; additionally, as a high spin d^5 system, *d-d* transitions are both spin and Laporte forbidden, and would thus be very weak.[113] It has been shown that collecting the absorption spectra of various Fe(III) octahedral

complexes at low temperature, ca. 12 K, reveals *d-d* transitions ranging from ca. 450 to 1250 nm and charge transfer transitions from ca. 220 to 625 nm.[114] Even at these low temperatures, the intensity of the charge transfer transitions is far greater than that of the *d-d* transitions, and given the overlap of the regions it can be presumed that charge transfer transitions would dominate at room temperature and thereby obscure any weak *d-d* transitions.[113,114] For Fe(II) in a 6-coordinate environment, charge transfer transitions would again be the most likely suspect, the forbidden transitions rarely being observed.[113] However, in this case it would be a metal to ligand charge transfer (MLCT) as opposed to LMCT.[113] Thus it seems most likely that the observed feature in the case of the Fe-doped NCs is due to some sort of charge transfer transition. Collection of absorption spectra at low temperatures may aid in resolving this peak, thus enabling assignment of this transition. These findings also indicate that magneto-optical studies may be of interest for this system.

4.4 Magnetic Properties

In order to further assess the physical properties and ultimately the suitability of the Fe-doped In_2O_3 NCs for potential spintronics applications, magnetization measurements have been conducted on mildly annealed nanocrystalline thin films of the colloidal samples. Figure 4.8 shows the room temperature hysteresis loop measured for a 10% Fe-doped sample synthesized at 230 ^oC. While the signal-to-noise ratio is quite poor, this is not uncommon in such DMS-TCO materials; in this context, a strong signal would allude to a likely presence of magnetic secondary phases.

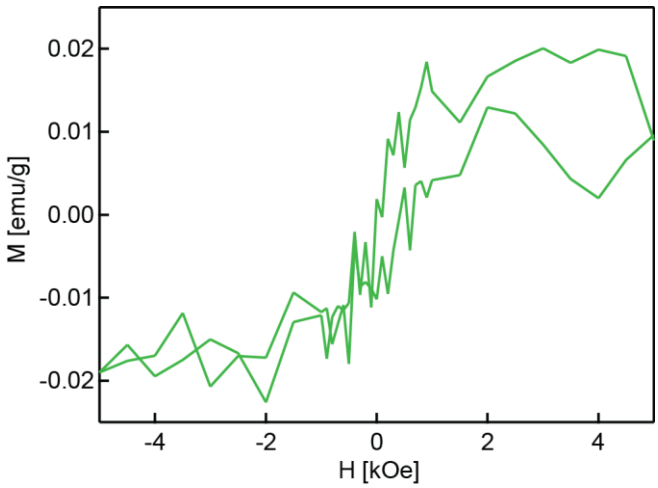

Figure 4.8: Magnetic hysteresis loop of an Fe-doped In_2O_3 nanocrystalline thin film collected at 300 K. The sample contains 10% Fe and was synthesized at an internal temperature ca. 230 ^{o}C.

Using the hysteresis loops and corresponding masses, the saturation magnetization, M_S, has been determined for each sample (Table 4.4).[115] It should be noted that the units emu/g refer to electromagnetic units per gram of sample, which includes Fe-doped In_2O_3, TOPO, and any trapped solvent molecules. In the calculation of M_S in terms of μ_B per Fe atom, it has been approximated that 50% of the sample mass can be accounted for as solvent and 30% as TOPO. This estimation is based on previous studies which found solvent and TOPO to be large contributors of mass, leaving ca. 20%, or even less, due to actual sample.

Table 4.4: Magnetization Saturation Determined for Fe-doped In_2O_3 Nanocrystalline Films

		Sample Mass [mg]	$M_S \times 10^{-3}$ [emu/g]	$M_S \times 10^{-2}$ [μ_B/Fe]
rh phase, 210 ^oC	5% Fe	3.67	6.35	6.22
		5.37	6.00	5.88
bcc phase, 230 ^oC	5% Fe	1.03	39.0	27.0
		1.90	7.34	5.08
		6.53	5.04	3.49
	10% Fe	1.73	17.7	3.81
		4.08	3.60	0.776
	15% Fe	1.90	19.8	2.99
		2.87	8.61	1.29

The replicate measurements of M_S for each sample were averaged and plotted as a function of the actual doping concentration (Figure 4.9). It can be seen that for bcc phase samples, the highest M_S is achieved with 1.77% doping, after which M_S decreases dramatically with increasing doping concentration. This is not unlike the Mn-doped In_2O_3 system, in which the maximum M_S was also observed with ca. 2% Mn and subsequently decreased with increasing Mn concentration.[70] This trend supports the conclusion that secondary phases are absent within the samples as increasing M_S with increasing doping concentration could suggest an extrinsic source of ferromagnetic behaviour.

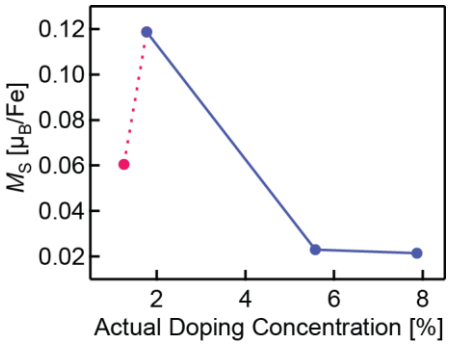

Figure 4.9: Plot of the saturation magnetization as a function of the actual doping concentration as determined through ICP-AES analysis. Blue dots indicate bcc phase samples; the pink dot indicates the rh phase sample. Lines serve as a guide to the eye, the dashed line indicating that this data point is still linked to the rest of the set, though it is of a different phase.

Using the available data, the mechanism of room temperature ferromagnetism observed in these particular samples can only be speculated on; further characterization is essential in order to draw concrete conclusions. Given the relatively low doping concentrations of all samples and the nature of such DMO materials, it is postulated that the observed ferromagnetic behaviour is induced by interfacial defects, as was the case for Cr-doped In_2O_3.[92] It is also likely that oxygen vacancies play a role since the relatively mild annealing conditions serve to fuse NCs and increase magnetic domains without inducing phase changes, and thus presumably minimizing incorporation of additional oxygen atoms in the process. Knowing that multiple oxidation states are present in the samples, a charge transfer mechanism as was seen in the Mn-doped system[70] could be at work; however, weak ferromagnetism was also observed in the sample containing only Fe^{3+}, thus making this possibility seem somewhat less likely. Considering the relationship between doping concentration and observed M_S, it is presumed that as the concentration of Fe increases, more Fe atoms occupy closer proximity sites and the exchange interaction changes; as a result, antiferromagnetic coupling would then become more common than ferromagnetic interactions, thus competing with and effectively reducing the measured M_S.[86]

Chapter 5 – Conclusions and Future Work

5.1 Conclusions Pertaining to Phase Transformation and Dopant Studies

5.1.1 Phase Transformation of Colloidal Indium Oxide Nanocrystals

The kinetics of *in situ* phase transformation during the growth of colloidal In_2O_3 NCs have been investigated. The coexistence of two distinct mechanisms of phase transformation were identified; the mechanism initiated by the nucleation of a new phase on the surface of individual NCs (SN), and at the interface between contacting NCs (IN). It is likely that high energy defect sites play an important role in enabling both mechanisms. It has been shown that through the control of temperature and precursor to solvent ratio, the mechanism of phase transformation can be controlled and systematically varied from pure SN to IN by increasing the aforementioned parameters. As a result, the contribution of different mechanisms to the phase transformation occurring under different synthetic conditions has been mapped. The two mechanisms are characterized by similar activation energy, ca. 150 kJ/mol. SN is found to be a predominant mechanism at lower temperatures, which is opposite from the trend reported for the phase transformation of TiO_2 NCs in the powder form. It is proposed that the change from SN to IN with increasing temperature is at least partly associated with increasing NC interactions, arising from Brownian motion. The complete phase transformation by SN at low temperatures can still be achieved kinetically over a longer time scale. Comparison with the TiO_2 nanopowder phase transformation results suggests that the activation energies are determined by local metal-oxygen bond rearrangement, rather than macroscopic properties of the polymorphic materials. It is plausible that other, more complex mechanisms of phase transformation are also possible under certain conditions, which represents an interesting topic for future investigations. The results of this work have general applicability, opening the doors for the examination of other colloidal polymorphic systems and the possibility of tailoring the properties of such materials for specific applications via structural transformations.

5.1.2 Iron-Doping of Colloidal Indium Oxide Nanocrystals

Nanocrystalline Fe-doped In_2O_3 has been successfully synthesized in colloidal solution and characterized in the context of examining the relationship between NC phase, growth, and doping concentration. Basic characterizations have shown that these species exhibit properties distinct from previously studied TM-doped In_2O_3 NCs, specifically Cr- and Mn-doped systems. Structural characterization using XRD patterns and TEM imaging indicated that increasing the doping concentration and temperature both resulted in increased particle size, which in turn lead to larger populations of bcc phase NCs as the critical size for phase transformation was reached and exceeded. rh NCs were only achieved through low doping, low temperature conditions. By contrast, Cr- and Mn-doped systems displayed an increasing population of small rh NCs as the doping concentration was increased. Analysis of the actual doping concentration via ICP-AES revealed that though the doping concentrations were significantly reduced from the intended amounts, the relative fraction of Fe incorporated increased with increasing starting amounts. Similar actual amounts of Fe for bcc and rh NCs synthesized with the same intended doping concentration suggested that Fe is nearly equally soluble in either lattice, the bcc phase being slightly preferred. Taken together, these results indicate that Fe as a dopant does not behave as anticipated, preferring the bcc phase host over rh-In_2O_3.

Spectroscopy was employed to gain further insight into the structural and electronic properties of the Fe-doped NCs. Through analysis of Fe K-edge XANES spectra and specifically the pre-edge feature, it was revealed that despite use of an Fe(III) precursor, three of four samples contained ca. 10% Fe^{2+}, indicating a reduction process during synthesis. This was also observed in Mn-doped In_2O_3, however the mixture of oxidation states was more dramatic in that case as both Mn^{2+} and Mn^{3+} were quite abundant. Comparison of the Fe K-edge XANES with that of the reference spectra confirmed the absence of secondary phases. Pre-edge analysis also alluded to increased disorder in the Fe-doped rh-In_2O_3 lattice compared to all bcc phase samples, suggesting b-site incorporation of dopants within the bcc lattice through comparison of site symmetries. UV-vis spectroscopy confirmed a blue shift in the band gaps of all samples, indicating quantum confinement. Concentrated colloidal solutions exhibit a weak transition at ca. 478 nm; it was determined that this is most likely a charge transfer transition.

This preliminary look at the structure and properties of colloidal Fe-doped In_2O_3 NCs culminated with magnetization measurements, demonstrating that the mildly annealed nanocrystalline films were weakly ferromagnetic at room temperature. The highest M_S was achieved with ca. 2% Fe actual doping concentration in a bcc phase sample. While additional experiments are required to unambiguously establish the origin of this ferromagnetic behaviour, it was presumed that an interfacial defect mediated mechanism likely dominates up until a critical doping concentration, after which point antiferromagnetic interactions become more abundant and result in a decrease in saturation magnetization.

5.2 Future Work and Possible Research Directions

5.2.1 Phase Transformation and Colloidal Systems

Given the significant steps that have been taken in advancing understanding of phase transformation in colloidal In_2O_3 NCs, a number of distinct and challenging future research directions arise as a result. In this work, the IN and SN mechanisms have been thoroughly studied and the conditions under which each takes place, either individually or simultaneously, have been identified. Exploration of a phase transformation mechanism involving nucleation of a new phase assisted by a ligand, such as oleylamine, would be unique to colloidal systems. This would be a very difficult scenario to model theoretically as it would require consideration of many factors, such as, but certainly not limited to, how the ligand could bind to the NC surfaces and possible resulting bond rearrangements which could lead to the new phase. These kinds of studies would be influential since the majority of phase transformation studies focus on the solid state, or else use models originally designed for solid state systems in the powder form.

An alternative route to continue phase transformation studies would be through assessment of different colloidal metal oxide systems, such as vanadium oxide. This would pose different challenges since systems such as vanadium oxide have not only multiple phases, but different oxidation states and chemical compositions that accompany them.

Lastly, an additional research option and possibly the most intuitive direction would be to perform similar studies using colloidal indium oxide as demonstrated in this work, but with the

addition of dopants. This would delve deeper into the relationship between the dopant-host lattice interactions during NC nucleation, growth, and phase transformation. However, these studies would again pose many challenges since a large number of variables are in effect; temperature, precursor to solvent ratio, synthesis time, concentration of dopant, and species of dopant. This would therefore have to be a highly systematic study in order to maintain control of the many variables, but despite the challenges it would be informative and shed more light on processes in colloidal nanocrystalline systems.

5.2.2 Colloidal Iron-Doped Indium Oxide and Other Dopant Systems

While much characterization and analysis of Fe-doped In_2O_3 NCs has been done, some highly informative experiments and analysis have yet to be completed. As mentioned in section 4.3.1, collection of additional XAS spectra of various standards, such as, but not limited to, FeO and Fe_2O_3, would be highly beneficial for both XANES and future EXAFS analyses. Additional standards would increase confidence in confirming the absence of secondary phases via either of these analytical techniques, and in the case of XANES it would provide more standards for the calibration curve in determination of the oxidation states. Along these lines, synthesis of Fe-doped In_2O_3 using a precursor containing Fe^{2+} would pose an interesting study as the ratios of Fe^{3+} and Fe^{2+} may or may not change as a result, thereby potentially affecting other physical properties of the NCs. This additional work would then increase the value of experiments such as X-ray photoelectron spectroscopy or Mössbauer spectroscopy, which would unambiguously establish the ratios of Fe^{2+} to Fe^{3+} in the NCs. Another experiment of interest would be to attempt nominal doping concentrations lower than 5% Fe, such as 2% Fe. With such low doping concentrations, it might be possible to isolate more rh samples and thus provide more of a comparison for the samples investigated in this work.

As discussed in section 4.3.1, analysis of the EXAFS spectra collected for these samples would be a beneficial study as it could confirm the coordination number of the Fe absorber, determine the bond distances and thus aid in identification of dopant sites, and clearly identify any possible secondary phases. In order to enable this, more scans of the EXAFS region should be collected and merged with existing spectra; this will provide a higher quality average of the

data, which is critical in order to properly analyze the subtle oscillations, particularly at the higher energy regions.

Another important future experiment involves the use of magnetic circular dichroism (MCD), a spectroscopic technique which measures the differential absorption of left and right circularly polarized light (lcp and rcp, respectively) in the presence of an external magnetic field.[116] While chiral molecules naturally exhibit circular dichroism in the absence of a magnetic field, materials can be induced into absorbing lcp and rcp to different extents when a magnetic field is applied and the Faraday effect is observed in these low temperature experiments.[116] The magnetic field causes degenerate states to split, a phenomenon known as the Zeeman effect[117], and transitions from the ground to excited states are governed by whether the absorbed light is lcp or rcp. This measurement is complementary to absorption spectroscopy, providing ground and excited electronic state information for a given species in the presence of a magnetic field via assignment of the high resolution transitions.[118] The advantage of this technique over similar methods, such as electron paramagnetic resonance, is that it allows excited states to be probed as opposed to only the ground state. In the case of Fe-doped In_2O_3 NCs, this technique could prove to be an interesting course of study considering the observation of a weak but broad charge transfer transition in the absorption spectra. MCD studies could resolve this feature and enable assignment of spectral transitions, ultimately providing information regarding the electronic structure of Fe in In_2O_3 as well as the magnetic interactions of the dopant and host via examination of MCD field dependence as was done in the case of Mn-doped In_2O_3.[70]

In addition to completion of studies with Fe, other TM dopants systems such as Ni- and Co-doped In_2O_3 NCs would be worth exploring in the same context as has been done with Fe. Given how different Fe has proven to be from previously studied Cr- and Mn-doped In_2O_3 systems, utilization of additional TMs would reveal more information about how the different dopants interact with the host lattice in the context of NC growth and phase transformation. As well, with a variety of TM dopants studied, periodic trends in material characteristics may become apparent. These studies would also be of importance as they would enable identification of the most promising systems for potential spintronics applications, while simultaneously developing ways to further tailor these materials for specific needs.

APPENDIX A: PHASE TRANSFORMATION OF PURE INDIUM OXIDE

Synthesis with precursor to solvent ratio 1:20 at 188 ^{o}C yielded only a negligible amount of bcc-In_2O_3 as determined by linear combination of XRD patterns. However, the formation of rh-In_2O_3 NCs from InOOH was observed, as shown in Figure A1. This observation provides supporting evidence for the dehydration mechanism of the formation of In_2O_3 NCs, in addition to demonstrating that rh-In_2O_3 is a transitory phase between the InOOH precursors and the stable bcc-In_2O_3 NCs.

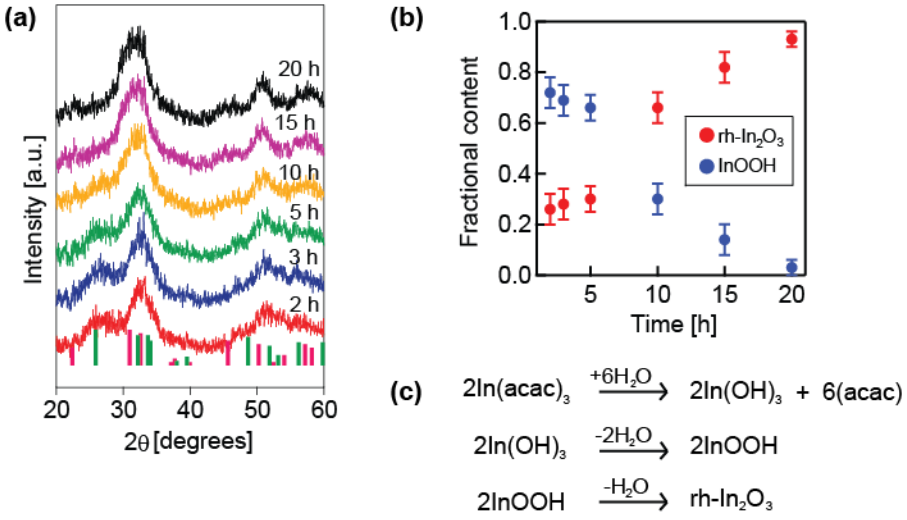

Figure A1. (a) XRD patterns of samples isolated in the synthesis with 1:20 precursor to solvent ratio at 188 ^{o}C over the course of 20 h. Green sticks indicate InOOH, while pink sticks indicate rh-In_2O_3 pattern. (b) Fractional content evolution based on the linear combination analysis of the XRD patterns over time. The InOOH fractional content decreases while that of rh-In_2O_3 increases, supporting that rh-In_2O_3 NCs form via dehydration of InOOH. (c) Balanced reaction scheme outlining the formation of rh-In_2O_3 NCs from $In(acac)_3$ precursors.

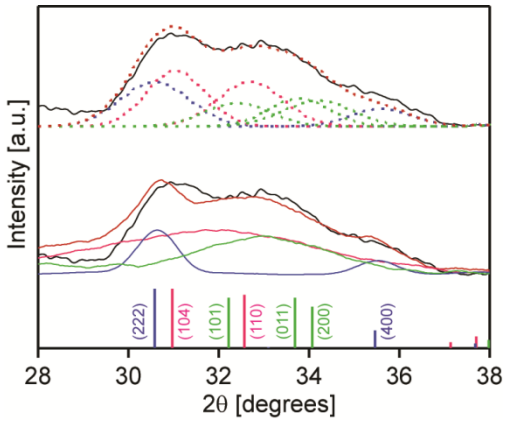

Figure A2. Experimental XRD pattern (black lines), together with the linear combination (bottom) and peak deconvolution (top) analysis for a 2 h sample from the 1:20 precursor to solvent series at 200 ^{o}C. Experimental XRD patterns of reference InOOH, rh-In_2O_3, and bcc-In_2O_3 NCs for linear combination analysis are shown in green, pink, and blue, respectively, and the resulting linear combination pattern is shown in orange. The same colors but dashed lines are used for showing the deconvolution analysis. Bulk reference patterns for InOOH, rh-In_2O_3, and bcc-In_2O_3 are shown by green, pink, and blue sticks, respectively.

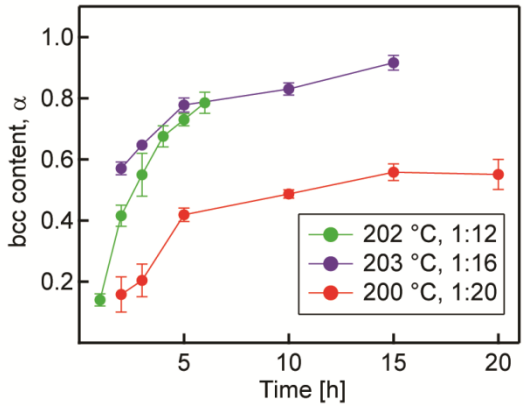

Figure A3. Fractional bcc-In_2O_3 phase content at constant temperature (ca. 200 ^{o}C) for different precursor to solvent ratios.

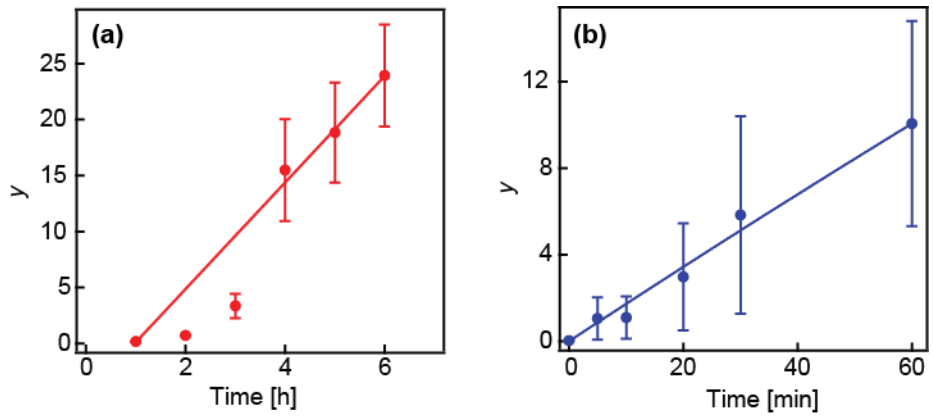

Figure A4. *y* vs *t* plots of samples synthesized at (a) 202 °C and (b) 212 °C with a precursor to solvent ratio of 1:12, as the most concentrated series. These data were best fit with the ideal IN model (see ref. 32 for details).

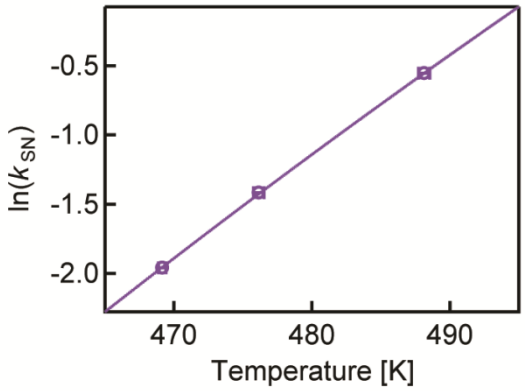

Figure A5. Arrhenius plot for the data derived from the sample series prepared using 1:16 precursor to solvent ratio. Solid line is the best fit to data points using eq 1.6 in the main text. From the fitting of these data, E_a(SN) was found to be ca. 140 kJ/mol and A_o(SN) is 6.1×10^{14} h^{-1} (1.7×10^{11} Hz).

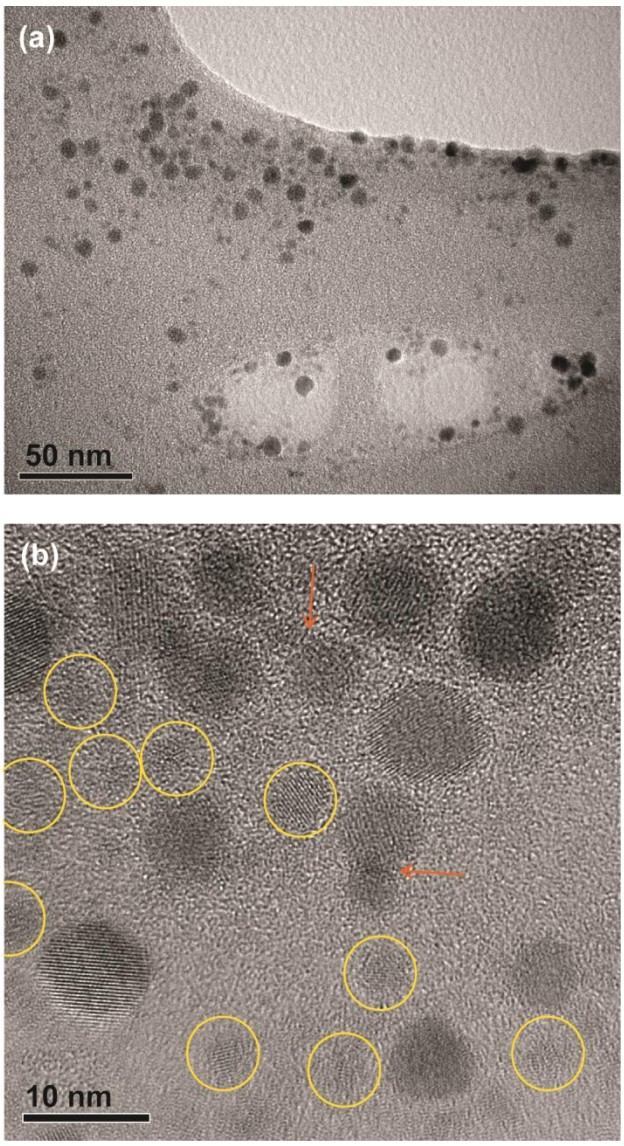

Figure A6. (a) Overview TEM image of In_2O_3 NCs synthesized at 200 °C using 1:20 precursor to solvent ratio, 5 h after reaching the final reaction temperature. (b) Magnified TEM image of the same NCs. Circles indicate representative NCs that are definitively smaller than 5 nm, while arrows indicate dumbbell-shaped NCs formed by contacting two smaller NCs.

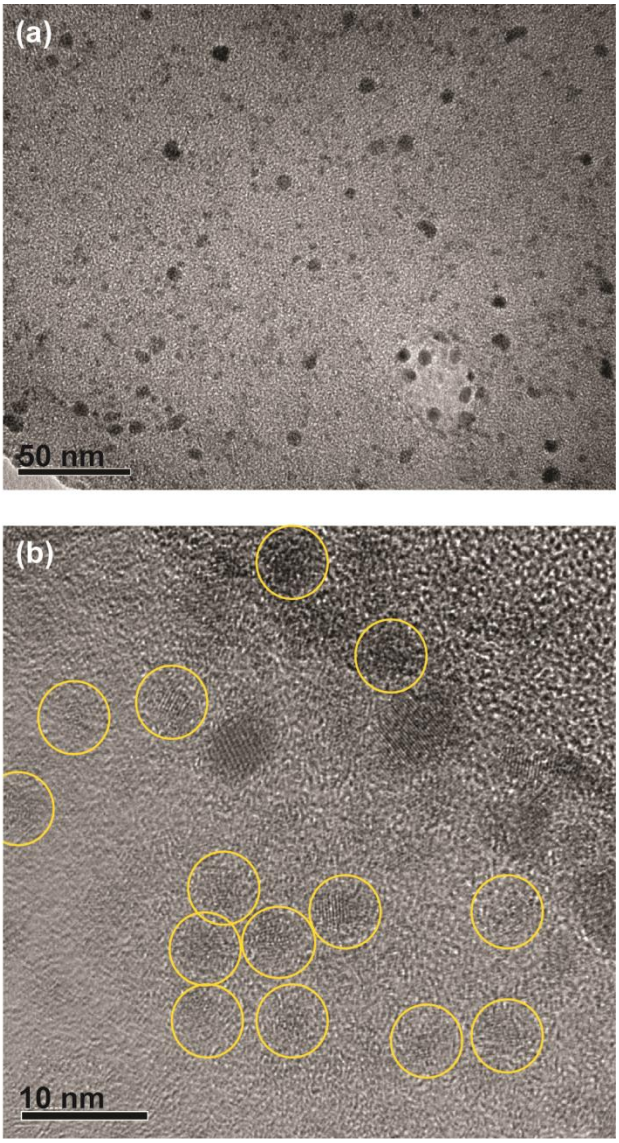

Figure A7. (a) Overview TEM image of In_2O_3 NCs synthesized at 200 °C using 1:20 precursor to solvent ratio, 3 h after reaching the final reaction temperature. (b) Magnified TEM image of the same NCs. Circles indicate representative NCs that are definitively smaller than 5 nm.

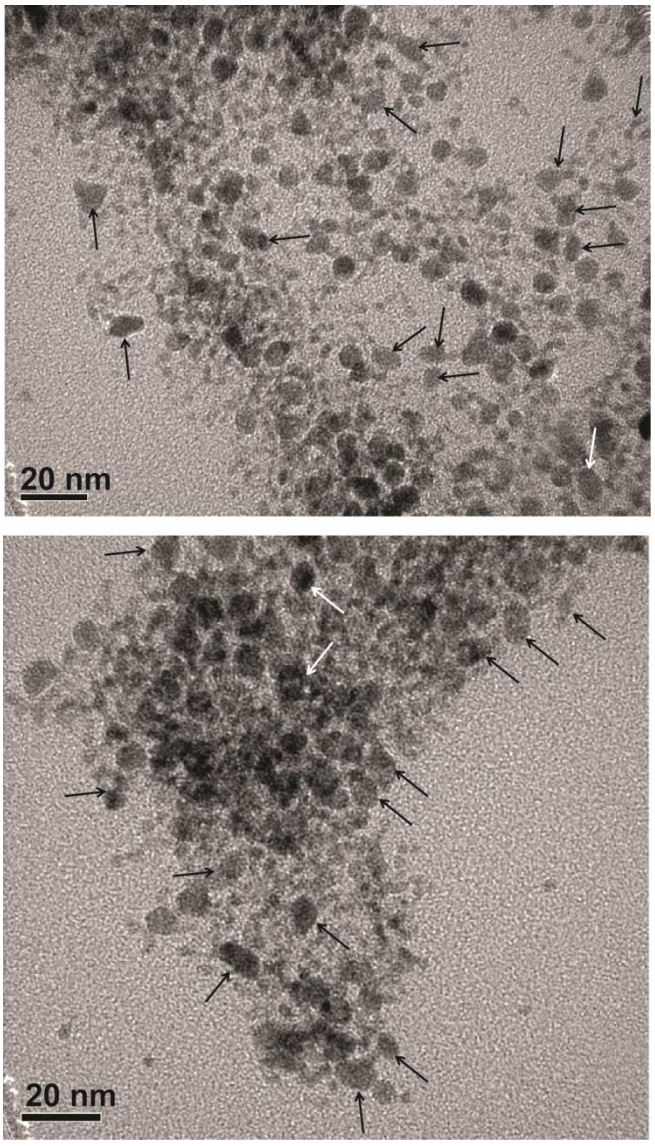

Figure A8. (a) Overview TEM image of In_2O_3 NCs synthesized at 200 °C using 1:12 precursor to solvent ratio, 1 h after reaching the final reaction temperature. Arrows indicate representative NCs that have elliptical or dumbbell morphology.

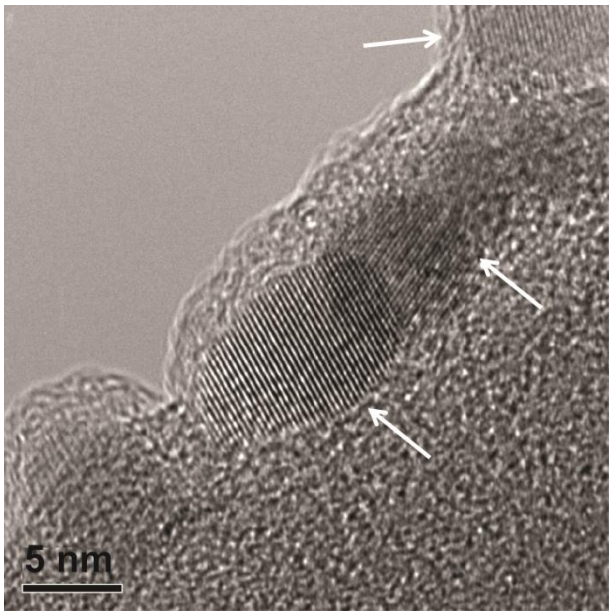

Figure A9. (a) High resolution TEM image of In_2O_3 NCs synthesized at 200 °C using 1:12 precursor to solvent ratio, 1 h after reaching the final reaction temperature. Arrows indicate representative NCs that have elliptical or dumbbell morphology. These NCs have bcc-In_2O_3 structure, consistent with IN mechanism.

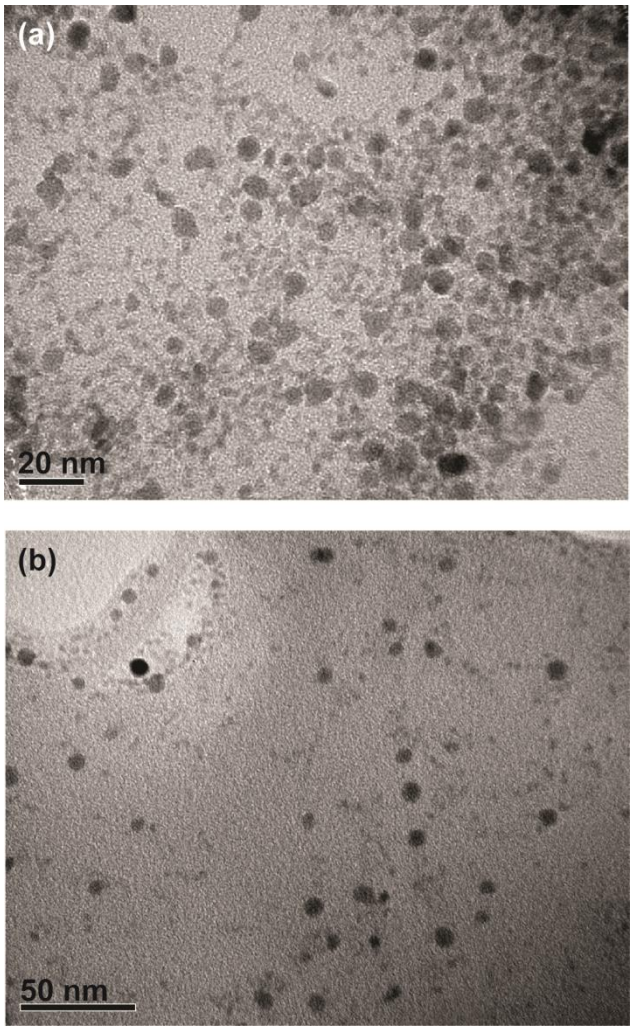

Figure A10. Overview TEM image of In_2O_3 NCs synthesized at 200 °C with (a) 1:12 precursor to solvent ratio, 1 h after reaching the final reaction temperature, and (b) 1:20 precursor to solvent ratio 3 h after reaching the final reaction temperature. The NC sizes and relative ratio of small to large NCs is similar in both images, but the reaction yield and the number of NCs are much larger for 1:12 samples, consistent with higher probability of NC contact formation characteristic for IN mechanism.

Table A1: Determining bcc Phase Content Using Deconvolution and Linear Combination Methods for Samples Synthesized with Precursor to Solvent Ratio 1:20

	Time [h]	Deconvolution	Linear Combination	Average bcc Content
200 ^{o}C	2	0.21	0.10	0.16
	3	0.26	0.16	0.21
	5	0.40	0.44	0.42
	10	0.47	0.50	0.48
	15	0.53	0.58	0.56
	20	0.50	0.60	0.55
206 ^{o}C	2	0.40	0.40	0.40
	3	0.58	0.60	0.59
	5	0.61	0.70	0.65
	10	0.83	0.86	0.84
	15	0.83	0.93	0.88
	20	0.85	0.94	0.90
211 ^{o}C	2	0.43	0.48	0.45
	3	0.55	0.67	0.61
	5	0.66	0.72	0.70
	10	0.61	0.74	0.67
	15	0.67	0.76	0.72
	20	0.68	0.80	0.74
215 ^{o}C	2	0.66	0.55	0.60
	3	0.70	0.75	0.72
	5	0.79	0.88	0.83
	10	0.86	0.95	0.90
	15	1.00	1.00	1.00
	20	1.00	1.00	1.00
224 ^{o}C	2	0.68	0.74	0.71
	3	0.87	0.91	0.89
	5	0.91	0.94	0.92
	10	0.88	0.97	0.93
	15	1.00	1.00	1.00
	20	1.00	1.00	1.00

Table A2: Comparing Adjusted R^2 Values from Fitting Data with Different Models

	T [^{o}C]	Model	R^2
1:20	200	y(SN)	0.9819
		y(IN+SN)	0.9949
	206	y(SN)	0.8754
		y(IN+SN)	0.9991
	215	y(SN)	0.9824
		y(IN+SN)	0.9979
	224	y(IN)	0.9641
1:16	196	y(SN)	0.9576
		y(IN+SN)	0.9367
	203	y(SN)	0.9932
		y(IN+SN)	0.9919
	215	y(IN)	0.8342
1:12	202	y(IN)	0.9106
	212	y(IN)	0.9805

APPENDIX B: IRON-DOPED INDIUM OXIDE STUDIES

As a preliminary confirmation that secondary phases are absent from the Fe-doped In_2O_3 samples, experimental XRD patterns were compared with various iron oxide reference patterns (Figure B1). It can be seen that the only overlap of reference peaks with the experimental pattern for 5% Fe, ca. 230 ^{o}C occurs at ca. 35 ^{o}, however none of the other iron oxide reference peaks line up with either of the experimental patterns. Thus it was concluded that amounts of secondary phases within the detection range of XRD do not exist in these samples.

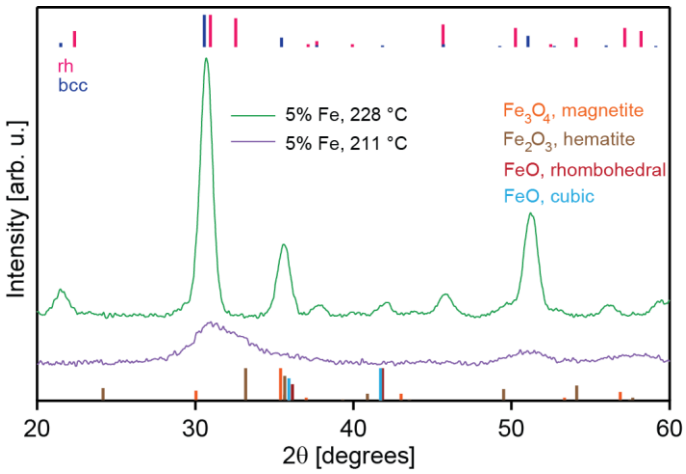

Figure B1. Comparing 5% Fe doped samples synthesized at 211 ^{o}C (purple) and 228 ^{o}C (green) with the reference peaks of various iron oxides (bottom) and the rh and bcc phases of indium oxide (top).

In order to correlate the Fe-doped samples of this work with doped In_2O_3 NCs synthesized in previous studies and preliminary experiments, it was necessary to establish the approximate relationship between internal and external synthesis temperature. This is shown schematically in Figure B2 below. The typical error in temperature is again ca. ± 2.5 ^{o}C, as was established in the phase transformation studies of pure In_2O_3 NCs.

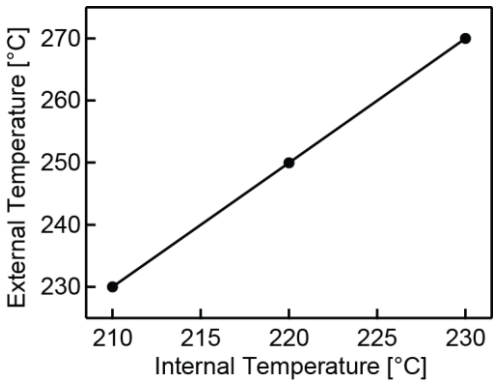

Figure B2. Demonstration of the linear relationship between internal and external temperature in concentrated (precursor to solvent ratio 1:12) Fe-doped In_2O_3 NC synthesis. Line serves as a guide to the eye.

The pre-edge centroid is calculated using the positions of the fitted peaks, which are weighted using the respective integrated intensities, in order to find the average energy position of the pre-edge feature. This calculation is demonstrated below using data from the first scan of the 5% Fe, 210 ^{o}C sample. Let a_i represent the area and p_i the position of peak i, and let C represent the centroid of the sample.

$a_1 = 0.03352$
$p_1 = 7113.540$
$a_2 = 0.10233$
$p_2 = 7114.706$

$$C = \frac{\sum_{i=1} a_i p_i}{\sum_{i=1} a_i} = \frac{(a_1 p_1) + (a_2 p_2)}{(a_1 + a_2)}$$

$$= \frac{(0.03352)(7113.540\ \text{eV}) + (0.10233)(7114.706\ \text{eV})}{(0.03352) + (0.10233)}$$

$$= 7114.418298\ \text{eV}$$

$$\cong 7114.42\ \text{eV}$$

Thus, the centroid of the first scan for the 5% Fe, 210 ^{o}C sample is 7114.42 eV.

Table B1 below summarizes the results of the XANES pre-edge fitting performed on Fe-doped samples as well as the hematite and olivine reference materials.

Table B1: XANES Fe K-edge Analysis – Pre-edge Fitting Results

		Peak Area	Peak Location [eV]	Total Area	Centroid [eV]	R^2
Olivine		0.0195	7112.26	0.0506	7113.18	0.9901
		0.0155	7113.13			
		0.0155	7114.38			
Hematite		0.0114	7113.64	0.0310	7114.49	0.9934
		0.0195	7114.98			
5% Fe, 210 ^{o}C	Scan 1	0.0335	7113.54	0.1358	7114.42	0.9904
		0.1023	7114.70			
	Scan 2	0.0267	7113.21	0.1097	7114.30	0.9906
		0.0830	7114.66			
5% Fe, 230 ^{o}C	Scan 1	0.0071	7112.97	0.0828	7114.38	0.9961
		0.0481	7114.12			
		0.0300	7115.15			
	Scan 2	0.0197	7113.11	0.0960	7114.30	0.9925
		0.0449	7114.17			
		0.0344	7115.15			
15% Fe, 210 ^{o}C	Scan 1	0.0091	7112.69	0.0907	7114.32	0.9933
		0.0474	7114.08			
		0.0343	7115.09			
15% Fe, 230 ^{o}C	Scan 1	0.0512	7114.05	0.0918	7114.52	0.9926
		0.0406	7115.11			
	Scan 2	0.0570	7114.06	0.1009	7114.52	0.9942
		0.0439	7115.11			

Table B2 tabulates the ratios of $Fe^{3+}/\Sigma Fe$ estimated for the Fe-doped In_2O_3 samples through pre-edge analysis and use of the hematite and olivine standards.

Table B2: Estimated Ratios of $Fe^{3+}/\Sigma Fe$ Based on Analysis of the Centroid Position

Species	Centroid Position [eV]	$Fe^{3+}/\Sigma Fe$
Olivine	7113.18	0
Hematite	7114.49	1
5% Fe, 210 ^{o}C	7114.36	0.9008
5% Fe, 230 ^{o}C	7114.34	0.8855
15% Fe, 210 ^{o}C	7114.32	0.8702
15% Fe, 230 ^{o}C	7114.52	1.023

The X-ray absorption K-edges of the species studied in this work are tabulated below in Table B3. The edges were identified using first derivative plots of the XAS spectra. It can be seen that the edges of all samples lay between those of the reference minerals, indicating mixed valence of Fe.

Table B3: K-Edge Energies of Mineral References and Fe-doped In_2O_3 Samples

Species	Edge [eV]
Olivine	7125.85
Hematite	7129.12
5% Fe, 210 ^{o}C	7126.00
5% Fe, 230 ^{o}C	7126.57
15% Fe, 210 ^{o}C	7126.40
15% Fe, 230 ^{o}C	7127.16

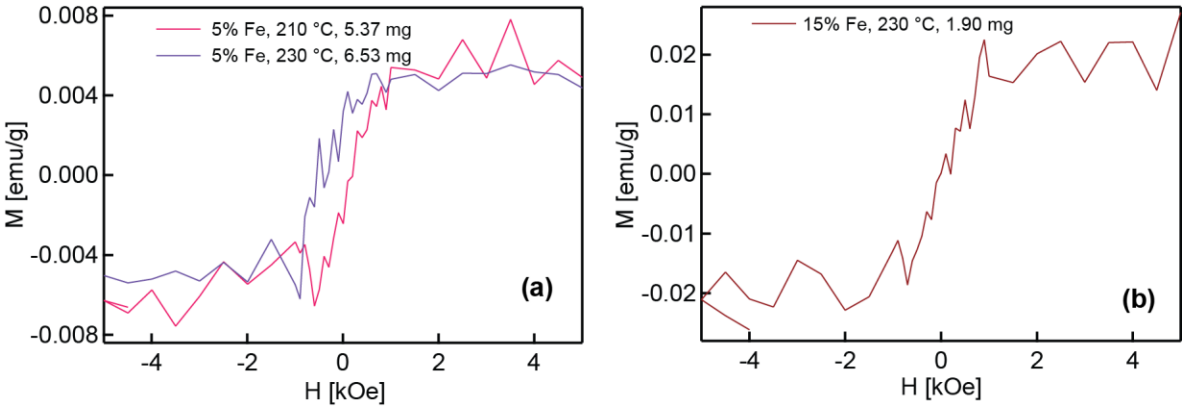

Figure B3. (a) Magnetic hysteresis loops of the 5% Fe doped samples synthesized at ca. 210 (pink) and 230 ^{o}C (purple), representing the rh and bcc phases, respectively. (b) Magnetic hysteresis loop collected for 15% Fe doped sample synthesized at ca. 230 ^{o}C, demonstrating that even though the magnetization is relatively weak, the distinctive hysteresis shape is present. All data were collected at 300 K, and the indicated masses are those of the specific sample measured.

PERMISSIONS

Title: Controlling the Mechanism of Phase Transformation of Colloidal In2O3 Nanocrystals

Author: Lisa N. Hutfluss, Pavle V. Radovanovic

Publication: Journal of the American Chemical Society

Publisher: American Chemical Society

Date: Jan 1, 2015

PERMISSION/LICENSE IS GRANTED FOR YOUR ORDER AT NO CHARGE

This type of permission/license, instead of the standard Terms & Conditions, is sent to you because no fee is being charged for your order. Please note the following:

- Permission is granted for your request in both print and electronic formats, and translations.
- If figures and/or tables were requested, they may be adapted or used in part.
- Please print this page for your records and send a copy of it to your publisher/graduate school.
- Appropriate credit for the requested material should be given as follows: "Reprinted (adapted) with permission from (COMPLETE REFERENCE CITATION). Copyright (YEAR) American Chemical Society." Insert appropriate information in place of the capitalized words.
- One-time permission is granted only for the use specified in your request. No additional uses are granted (such as derivative works or other editions). For any other uses, please submit a new request.

REFERENCES

(1) Kim, J. Y.; Voznyy, O.; Zhitomirsky, D.; Sargent, E. H. *Adv. Mater.* **2013**, *25*, 4986 - 5010.

(2) El-Sayed, M. A. *Acc. Chem. Res.* **2004**, *37*, 326 - 333.

(3) Robertson, J.; Gillen, R.; Clark, S. J. *Thin Solid Films* **2012**, *520*, 3714 - 3720.

(4) Radovanovic, P. V. In *Functional Metal Oxides*; Ogale, S. B., Venkatesan, T. V., Blamire, M. G., Eds.; Wiley-VCH Verlag GmbH & Co.: 2013.

(5) Hong, W.-K.; Park, J. B.; Yoon, J.; Kim, B.-J.; Sohn, J. I.; Lee, Y. B.; Bae, T.-S.; Chang, S.-J.; Huh, Y. S.; Son, B.; Stach, E. A.; Lee, T.; Welland, M. E. *Nano Lett.* **2013**, *13*, 1822 - 1828.

(6) Farvid, S. S.; Hegde, M.; Radovanovic, P. V. *Chem. Mater.* **2013**, *25*, 233 - 244.

(7) Zhang, H.; Banfield, J. F. *J. Mater. Chem.* **1998**, *8*, 2073 - 2076.

(8) Farvid, S. S.; Dave, N.; Radovanovic, P. V. *Chem. Mater.* **2010**, *22*, 9 - 11.

(9) Farvid, S. S.; Dave, N.; Wang, T.; Radovanovic, P. V. *J. Phys. Chem. C* **2009**, *113*, 15928 - 15933.

(10) Epifani, M.; Siciliano, P. *J. Am. Chem. Soc.* **2004**, *126*, 4078 - 4079.

(11) Lee, C. H.; Kim, M.; Kim, T.; Kim, A.; Paek, J.; Lee, J. W.; Choi, S. Y.; Kim, K.; Park, J. B.; Lee, K. *J. Am. Chem. Soc.* **2006**, *128*, 9326 - 9327.

(12) Gurlo, A. *Angew. Chem. Int. Ed.* **2010**, *49*, 5610 - 5612.

(13) Lu, Q.; Yun, G.; Zhou, W.; Li, J. *J. Mater. Sci. Technol.* **2013**, *29*, 841 - 845.

(14) Solozhenko, V. L.; Kurakevych, O. O.; Sokolov, P. S.; Baranov, A. N. *J. Phys. Chem. A* **2011**, *115*, 4354 - 4358.

(15) Zheng, P.; Hao, R.; Zhao, J.; Jia, S.; Cao, B.; Zhu, Z. *J. Mater. Chem. A* **2014**, *2*, 4907 - 4911.

(16) Prasad, K.; Pinjari, D. V.; Pandit, A. B.; Mhaske, S. T. *Ultrason. Sonochem.* **2010**, *17*, 409 - 415.

(17) Azizi, K. F.; Bagheri-Mohagheghi, M.-M. *J. Sol-Gel Sci. Technol.* **2013**, *65*, 329 - 335.

(18) Bergerud, A.; Buonsanti, R.; Jordan-Sweet, J. L.; Milliron, D. J. *Chem. Mater.* **2013**, *25*, 3172 - 3179.

(19) Wang, T.; Chirmanov, V.; Chiu, W. H. M.; Radovanovic, P. V. *J. Am. Chem. Soc.* **2013**, *135*, 14520 - 14523.

(20) Jiang, F.-X.; Xu, X.-H.; Zhang, J.; Fan, X.-C.; Wu, H.-S.; Alshammari, M.; Feng, Q.; Blythe, H. J.; Score, D. S.; Addison, K.; Al-Qahtani, M.; Gehring, G. A. *J. Appl. Phys.* **2011**, *109*, 053907.

(21) Wan, Q.; Dattoli, E. N.; Fung, W. Y.; Guo, W.; Chen, Y.; Pan, X.; Lu, W. *Nano Lett.* **2006**, *6*, 2909 - 2915.

(22) Fortunato, E.; Ginley, D.; Hosono, H.; Paine, D. C. *MRS Bull.* **2007**, *32*, 242 - 247.

(23) Zhuang, Z.; Peng, Q.; Liu, J.; Wang, X.; Li, Y. *Inorg. Chem.* **2007**, *46*, 5179 - 5187.

(24) Gurlo, A.; Kroll, P.; Riedel, R. *Chem. Eur. J.* **2008**, *14*, 3306 - 3310.

(25) Karazhanov, S. Z.; Ravindran, P.; Vajeeston, P.; Ulyashin, A.; Finstad, T. G.; Fjellvag, H. *Phys. Rev. B* **2007**, *76*, 075129.

(26) Shannon, R. D. *Solid State Commun.* **1966**, *4*, 629 - 630.

(27) Jiang, H.; Zhao, L.; Gai, L.; Ma, L.; Ma, Y.; Li, M. *Cryst. Eng. Comm.* **2013**, *15*, 7003 - 7009.

(28) Solieman, A.; Zayed, M. K.; Alamri, S. N.; Al-Dahoudi, N.; Aegerter, M. A. *Mater. Chem. Phys.* **2012**, *134*, 127 - 132.

(29) Jiang, Q.; Liang, L. H.; Zhao, D. S. *J. Phys. Chem. B* **2001**, *105*, 6275 - 6277.

(30) Vlasov, N. M.; Dragunov, Y. G. *Tech. Phys.* **2013**, *58*, 218 - 222.

(31) Zatryb, G.; Podhorodecki, A.; Misiewicz, J.; Cardin, J.; Gourbilleau, F. *Nanoscale Res. Lett.* **2013**, *8*, 40 - 46.

(32) Farvid, S. S.; Radovanovic, P. V. *J. Am. Chem. Soc.* **2012**, *134*, 7015 - 7024.

(33) Shekar, N. V. C.; Rajan, K. G. *Bull. Mater. Sci.* **2001**, *24*, 1 - 21.

(34) Gupta, D. C.; Rana, P. *J. Mol. Model.* **2012**, *18*, 3341 - 3350.

(35) Wu, H.; Wang, Z.; Fan, H. *J. Am. Chem. Soc.* **2014**, *136*, 7634 - 7636.

(36) Fontaine, D. D.; Paton, N. E.; Williams, J. C. *Acta Metall.* **1971**, *19*, 1153 - 1162.

(37) Zhang, H.; Banfield, J. F. *J. Mater. Res.* **2000**, *15*, 437 - 448.

(38) Embden, J. v.; Sader, J. E.; Davidson, M.; Mulvaney, P. *J. Phys. Chem. C* **2009**, *113*.

(39) Malek, J.; Mitsuhashi, T.; Criado, J. M. *J. Mater. Res.* **2001**, *16*, 1862 - 1871.

(40) Raju, S.; Mohandas, E. *J. Chem. Sci.* **2010**, *122*, 83 - 89.

(41) Villa, E.; Rios, P. R. *Acta Mater.* **2010**, *58*, 2752 - 2768.

(42) Vyazovkin, S.; Wight, C. A. *Annu. Rev. Phys. Chem.* **1997**, *48*, 125 - 149.

(43) Khawam, A.; Flanagan, D. R. *J. Phys. Chem. B* **2006**, *110*, 17315 - 17328.

(44) Avrami, M. *J. Chem. Phys.* **1939**, *7*, 1103 - 1112.

(45) Fanfoni, M.; Tomellini, M. *Nuovo Cimento Soc. Ital. Fis., D* **1998**, *20*, 1171 - 1182.

(46) Zhang, H.; Banfield, J. F. *Chem. Mater.* **2005**, *17*, 3421 - 3425.

(47) Engel, T.; Reid, P. *Thermodynamics, Statistical Thermodynamics, and Kinetics*; 2nd ed.; Pearson Prentice Hall: Upper Saddle River, NJ, 2010.

(48) O'Dwyer, C.; Szachowicz, M.; Visimberga, G.; Lavayen, V.; Newcomb, S. B.; Torres, C. M. S. *Nat. Nanotechnol.* **2009**, *4*, 239 - 244.

(49) Hamberg, I.; Granqvist, C. G. *J. Appl. Phys.* **1986**, *60*, R123 - R159.

(50) Wang, T.; Radovanovic, P. V. *J. Phys. Chem. C* **2011**, *115*, 406 - 413.

(51) Dederichs, P. H.; Sato, K.; Katayama-Yoshida, H. *Phase Transitions* **2005**, *78*, 851 - 867.

(52) Ohno, H. *Science* **1998**, *281*, 951 - 956.

(53) Coey, J. M. D. *Curr. Opin. Solid State Mater. Sci.* **2006**, *10*, 83 - 92.

(54) Zutic, I.; Fabian, J.; Sarma, S. D. *Rev. Mod. Phys.* **2004**, *76*, 323 - 410.

(55) West, A. R. *Basic Solid State Chemistry*; 2nd ed.; John Wiley & Sons: West Sussex, 2009.

(56) Zhang, Z. H.; Wang, X.; Xu, J. B.; Muller, S.; Ronning, C.; Li, Q. *Nat. Nanotechnol.* **2009**, *4*, 523 - 527.

(57) Ramasamy, K.; Sims, H.; Gupta, R. K.; Kumar, D.; Butler, W. H.; Gupta, A. *Chem. Mater.* **2013**, *25*, 4003 - 4009.

(58) Tanaka, K.; Fujita, K.; Nakashima, S.; Hojo, H.; Matoba, T. *J. Magn. Magn. Mater.* **2009**, *321*, 818 - 821.

(59) Sukegawa, H.; Mitani, S.; Niizeki, T.; Ohkubo, T.; Inomata, K.; Hono, K.; Shirai, M.; Miura, Y.; Abe, K.; Muramoto, S.; H01L 29/82 (2006.1) ed.; National Institute for Materials Science: United States, 2013; Vol. US 2013/0221461 A1.

(60) Brinkman, A.; Huijben, M.; Zalk, M. v.; Huijben, J.; Zeitler, U.; Maan, J. C.; Wiel, W. G. v. d.; Rijnders, G.; Blank, D. H. A.; Hilgenkamp, H. *Nature Mater.* **2007**, *6*, 493 - 496.

(61) Dietl, T. *Semicond. Sci. Technol.* **2002**, *17*, 377 - 392.

(62) Szotek, Z.; Temmerman, W. M.; Svane, A.; Petit, L.; Strange, P.; Stocks, G. M.; Kodderitzsch, D.; Hergert, W.; Winter, H. *J. Phys. Condens. Matter* **2004**, *16*, S5587 - S5600.

(63) Coey, J. M. D.; Chambers, S. A. *MRS Bull.* **2008**, *33*, 1053 - 1058.

(64) Hu, S.-J.; Yan, S.-S.; Lin, X.-L.; Yao, X.-X.; Chen, Y.-X.; Liu, G.-L.; Mei, L.-M. *Appl. Phys. Lett.* **2007**, *91*, 262514.

(65) Wang, V.; You, C.-Y.; He, H.-P.; Ma, D.-M.; Mizuseki, H.; Kawazoe, Y. *J. Magn. Magn. Mater.* **2013**, *348*, 55 - 60.

(66) Coey, J. M. D.; Venkatesan, M.; Fitzgerald, C. B. *Nat. Mater.* **2005**, *4*, 173 - 179.

(67) Qi, S.; Jiang, F.; Fan, J.; Wu, H.; Zhang, S. B.; Gehring, G. A.; Zhang, Z.; Xu, X. *Phys. Rev. B* **2011**, *84*, 205204.

(68) Coey, J. M. D.; Wongsaprom, K.; Alaria, J.; Venkatesan, M. *J. Phys. D: Appl. Phys.* **2008**, *41*, 134012.

(69) Jiang, Z.; Chen, S.; Zhang, D. *J. Phys. Chem. C* **2014**, *118*, 3789 - 3794.

(70) Farvid, S. S.; Sabergharesou, T.; Hutfluss, L. N.; Hegde, M.; Prouzet, E.; Radovanovic, P. V. *J. Am. Chem. Soc.* **2014**, *136*, 7669 - 7679.

(71) Xing, P. F.; Chen, Y. X.; Yan, S.-S.; Liu, G. L.; Mei, L. M.; Zhang, Z. *J. Appl. Phys.* **2009**, *106*, 043909.

(72) Datta, S.; Das, B. *Appl. Phys. Lett.* **1990**, *56*, 665 - 667.

(73) Dietl, T.; Ohno, H. *Rev. Mod. Phys.* **2014**, *86*, 187 - 251.

(74) Calle, C. d. l.; Martinez-Lope, M. J.; Pomjakushin, V.; Porcher, F.; Alonso, J. A. *Solid State Commun.* **2012**, *152*, 95 - 99.

(75) Meng, X.; Tang, L.; Li, J. *J. Phys. Chem. C* **2010**, *114*, 17569 - 17573.

(76) Sun, Q.; Zeng, Y.; Jiang, D. *Cryst. Eng. Comm.* **2012**, *14*, 713 - 718.

(77) Chu, D.; Zeng, Y.-P.; Jiang, D.; Ren, Z. *Appl. Phys. Lett.* **2007**, *91*, 262503.

(78) Kim, H.; Osofsky, M.; Miller, M. M.; Qadri, S. B.; Auyeung, R. C. Y.; Pique, A. *Appl. Phys. Lett.* **2012**, *100*, 032404.

(79) Singhal, A.; Achary, S. N.; Manjanna, J.; Jayakumar, O. D.; Kadam, R. M.; Tyagi, A. K. *J. Phys. Chem. C* **2009**, *113*, 3600 - 3606.

(80) Sun, Q.; Zeng, Y.; Jiang, D. *J. Nanopart. Res.* **2012**, *14*, 655.

(81) *CRC Handbook of Chemistry and Physics*; 95th ed., 2014 - 2015.

(82) Machala, L.; Tucek, J.; Zboril, R. *Chem. Mater.* **2011**, *23*, 3255 - 3272.

(83) Mou, X.; Wei, X.; Li, Y.; Shen, W. *Cryst. Eng. Comm.* **2012**, *14*, 5107 - 5120.

(84) Sakurai, S.; Namai, A.; Hashimoto, K.; Ohkoshi, S.-I. *J. Am. Chem. Soc.* **2009**, *131*, 18299 - 18303.

(85) Navrotsky, A.; Mazeina, L.; Majzlan, J. *Science* **2008**, *319*, 1635 - 1638.

(86) Xu, X.-H.; Jiang, F.-X.; Zhang, J.; Fan, X.-C.; Wu, H.-S.; Gehring, G. A. *Appl. Phys. Lett.* **2009**, *94*, 212510.

(87) Bérardan, D.; Guilmeau, E. *J. Phys. Condens. Matter* **2007**, *19*, 236224.

(88) Bérardan, D.; Guilmeau, E.; Pelloquin, D. *J. Magn. Magn. Mater.* **2008**, *320*, 983 - 989.

(89) Peleckis, G.; Wang, X. L.; Dou, S. X. *Appl. Phys. Lett.* **2006**, *88*, 132507.

(90) An, Y.; Wang, S.; Feng, D.; Wu, Z.; Liu, J. *Appl. Surf. Sci* **2013**, *276*, 535 - 538.

(91) It should be noted for comparison purposes that our previous work involving IN mechanism (see ref. 8 and 32) reported external rather than internal flask temperature, which was on average ca. 55 ^{o}C higher.

(92) Farvid, S. S.; Ju, L.; Worden, M.; Radovanovic, P. V. *J. Phys. Chem. C* **2008**, *112*, 17755 - 17759.

(93) Holzwarth, U.; Gibson, N. *Nat. Nanotechnol.* **2011**, *6*, 534.

(94) Wilke, M.; Farges, F.; Petit, P.-E.; Jr., G. E. B.; Martin, F. *Am. Mineral.* **2001**, *86*, 714 - 730.

(95) Petit, P.-E.; Farges, F.; Wilke, M.; Solé, V. A. *J. Synchrotron Radiat.* **2001**, *8*, 952 - 954.

(96) When fit with eq 1.4 (combined model), the obtained SN rate constant, k_{SN}, is nearly identical to that obtained from fitting with eq 1.3, while the IN term $k_{IN}N_o$ is nearly zero. This reinforces the identifcation of SN as the dominant mechanism of phase transformation in this case.

(97) As a check, the rearranged Arrhenius equation (eq 1.7) was utilized to estimate the activation energy using only two data points (see ref 37). In the case of the 1:20 dilution series, pairwise analysis using k_{SN} values and corresponding temperatures was completed using eq 1.7, the average of these results proving consistent with the full fitting. In the case of the 1:12 dilution series, E_a(IN) was calculated to be ca. 150 kJ/mol using eq 1.7, also illustrating consistency in the results.

(98) Penn, R. L.; Banfield, J. F. *Science* **1998**, *281*, 969 - 971.

(99) Shannon, R. D.; Pask, J. A. *J. Am. Chem. Soc.* **1965**, *48*, 391 - 398.

(100) Kumar, K. P.; Kelzer, K.; Burggraaf, A. J. *J. Mater. Chem.* **1993**, *3*, 1141 - 1149.

(101) Iida, Y.; Ozaki, S. *J. Am. Ceram. Soc* **1961**, *44*, 120 - 127.

(102) Gurlo, A.; Ivanovskaya, M.; Barsan, N.; Weimar, U. *Inorg. Chem. Commun.* **2003**, *6*, 569 - 572.

(103) Jiang, F.-X.; Feng, Q.; Quan, Z.-Y.; Ma, R.-R.; Heald, S. M.; Gehring, G. A.; Xu, X.-H. *Mater. Res. Bull.* **2013**, *48*, 3178 - 3182.

(104) Tandon, B.; Shanker, G. S.; Nag, A. *J. Phys. Chem. Lett.* **2014**, *5*, 2306 - 2311.

(105) Bunker, G. *Introduction to XAFS: A Practical Guide to X-ray Absorption Fine Structure Spectroscopy*; Cambridge University Press: New York 2010.

(106) Groot, F. d.; Vanko, G.; Glatzel, P. *J. Phys. Condens. Matter* **2009**, *21*, 104207.

(107) Berry, A. J.; O'Neill, H. S. C.; Jayasuriya, K. D.; Campbell, S. J.; Foran, G. J. *Am. Mineral.* **2003**, *88*, 967 - 977.

(108) Bajt, S.; Hanson, A. L. *Rev. Sci. Instrum.* **1995**, *66*, 1502 - 1504.

(109) An, Y.; Wang, S.; Feng, D.; Wu, Z.; Liu, J. *Appl. Phys. A* **2014**, *115*, 823 - 828.

(110) Sigrist, J. A.; Gaultois, M. W.; Grosvenor, A. P. *J. Phys. Chem. A* **2011**, *115*, 1908 - 1912.

(111) Berry, A. J.; Danyushevsky, L. V.; O'Neill, H. S. C.; Newville, M.; Sutton, S. R. *Nature* **2008**, *455*, 960 - 963.

(112) Stanek, C. R.; McClellan, K. J.; Uberuaga, B. P.; Sickafus, K. E.; Levy, M. R.; Grimes, R. W. *Phys. Rev. B* **2007**, *75*, 134101.

(113) Lever, A. B. P. *Inorganic Electronic Spectroscopy*; Elsevier Publishing Company: Amsterdam, The Netherlands, 1968.

(114) Kambli, U.; Gudel, H. U. *Inorg. Chem.* **1981**, *21*, 1270 - 1272.

(115) While most values of M_S are fairly similar between replicate samples and the overall data set, two appear to be potentially anomalous: the comparatively high M_S of 0.270 μ_B/Fe and low M_S of 0.00776 μ_B/Fe for the 5% and 10% Fe bcc phase samples, respectively. Performing the Q-test on these data indicates that these two questionable points should remain included in the set, however a boxplot suggests that 0.270 μ_B/Fe is an outlier. Considering that these methods of data evaluation should be utilized with caution, particularly when the data set is small, no data points will be excluded from subsequent analysis and discussion.

(116) Piepho, S. B.; Schatz, P. N. *Group Theory in Spectroscopy with Applications to Magnetic Circular Dichroism*; John Wiley and Sons: New York, 1983.

(117) Bransden, B. H.; Joachain, C. J. *Quantum Mechanics* 2nd ed.; Pearson Prentice Hall: Harlow, England, 2000.

(118) Ganyushin, D.; Neese, F. *J. Chem. Phys.* **2008**, *128*, 114117.